JACS
JOURNAL OF THE AMERICAN CHEMICAL SOCIETY
pubs.acs.org/JACS
Article

Stable Metal–Organic Electrocatalysts for Anion-Exchange Membrane Water Electrolyzers by Defect Engineering

Hongbin Xu,[○] Daniel J. Zheng,[○] Shuo Wang, Ethan Yupeng Zheng, Yilin Zhang, Tongchao Liu, Junxiang Liu, Davide Menga, Junghwa Kim, Jen-Hung Fang, Xiao Wang, Zhen Zhang, Lena Schröck, Jiaqi Wang, Sungsik Lee, Sunmoon Yu, Haldrian Iriawan, Guanzhou Zhu, Yuriy Román-Leshkov,* Ju Li,* and Yang Shao-Horn

Cite This: *J. Am. Chem. Soc.* 2025, 147, 29838–29851

Read Online

ACCESS | Metrics & More | Article Recommendations | Supporting Information

ABSTRACT: Developing efficient and durable catalysts for the alkaline oxygen evolution reaction (OER) is vital to achieving practical anion-exchange membrane water electrolyzers (AEMWEs) for green hydrogen production. Here, we break the activity–stability trade-off of electrocatalysis by defect engineering of Ni-based metal–organic electrocatalysts (Ni-benzenedicarboxylate; Ni-BDC) through coordinating ferrocenecarboxylates (Fc) to the metal sites. Experimental results collectively reveal that the defect MOF (Ni-BDC:Fc_5:1) exhibits a high OER turnover frequency of 0.75 O_2 s^{-1} at 300 mV overpotential. Operando Raman spectroscopy and isotope-labeling electrochemical mass spectrometry measurements indicate the structure of Ni-BDC:Fc_5:1 is also more stable in service than that of pure Ni-BDC. The high activity and stability could be attributed to the moderate defects (i.e., unsaturated Ni sites) in the structure that not only increase the intrinsic activity and stability of the local active environment by inhibiting lattice oxygen exchange but also electrochemically activate the bulk of the catalysts by creating a porous network that facilitates internal H_2O/OH^- conduction with enhanced electronic conduction. Accordingly, an AEMWE employing Ni-BDC:Fc_5:1 as the OER catalyst delivers an industrial-level current density of 1 A cm^{-2} at 1.73 V_{cell} and can be steadily operated for more than 120 h.

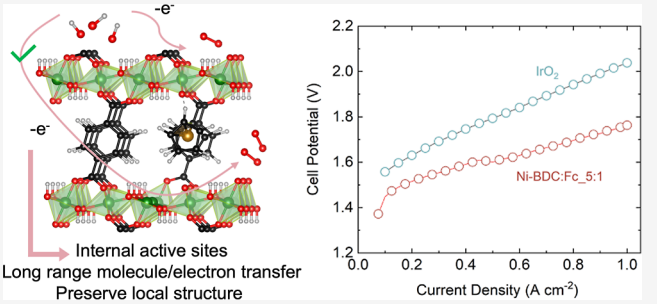

INTRODUCTION

Electrocatalytic water splitting is an appealing technology to store electrical energy in the chemical bonds of hydrogen and oxygen.[1,2] Anion-exchange membrane water electrolyzers (AEMWEs) possess the advantages of the low cost of alkaline water electrolysis and the high efficiency of zero-gap proton-exchange membrane water electrolyzers, making them a promising avenue for water splitting.[3,4] However, many catalysts suffer from a trade-off between activity and stability, limiting the practical application of AEMWE.[5−7] Thus, developing low-cost oxygen evolution reaction (OER) electrocatalysts with high, yet stable activity is crucial for green hydrogen production.

The activity and stability trade-off primarily arises from the intrinsic characteristics of the catalysts. Catalysts with structurally stable frameworks often exhibit inherently low intrinsic activities, whereas those with high activity may undergo rapid structural collapse during operation, leading to the inability to sustain the necessary conditions for catalytic reactions and, consequently, performance degradation.[8−11] Notably, structural changes during catalysis are not always undesirable; rather, the key question is whether the transformed structure can retain similar or even enhanced performance. Addressing this trade-off requires identifying the essential requirements for catalysis, which we believe include active sites, long-range percolating transport of reactants and products, and electron conduction. While maintaining the long-range ordered structure is ideal, preserving the local environment for transport and reaction is more crucial to ensuring performance stability, especially for real-world applications. Also, if bulk sites within the catalyst can participate in the reaction and the local active environment can be preserved over time, then the fundamental conditions for electrochemical reactions can be sustained even without long-range structural order.

Most current studies focus primarily on enhancing activity.[12−14] Nevertheless, the estimated turnover frequencies (TOFs), which serve as a measure of the intrinsic activity of

Received: April 11, 2025
Revised: July 27, 2025
Accepted: July 29, 2025
Published: August 11, 2025

https://doi.org/10.1021/jacs.5c06156
J. Am. Chem. Soc. 2025, 147, 29838–29851

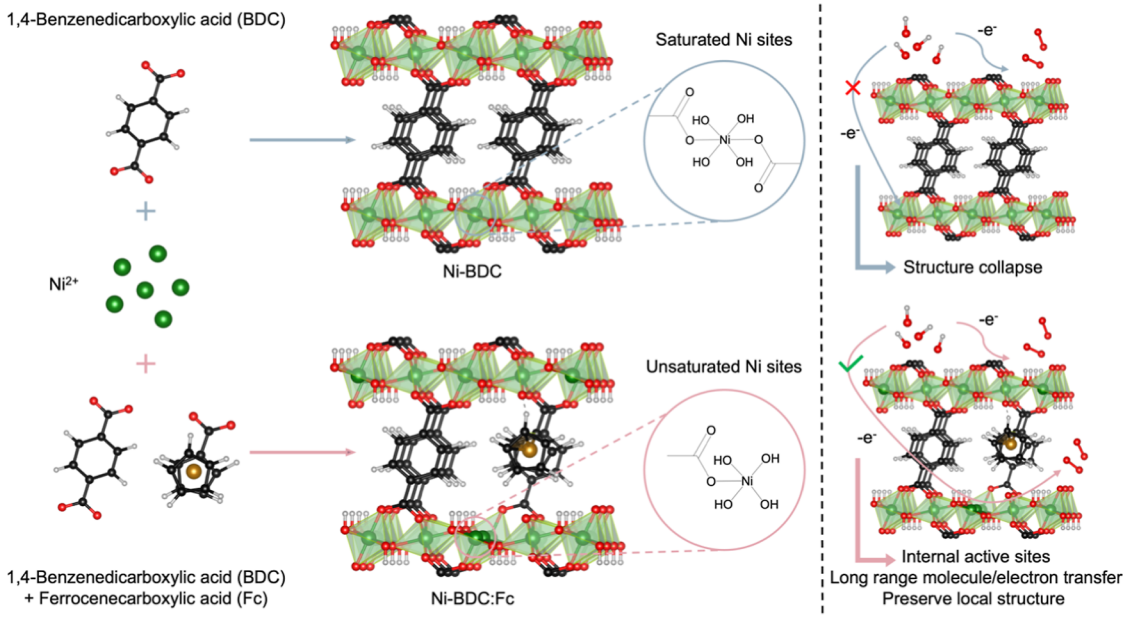

Figure 1. Catalyst design for defect engineering. Conventional Ni-BDC was synthesized using $NiCl_2$ as the metal precursor and BDC as the linker. The defect (unsaturated Ni sites) can be achieved by substituting some BDC linkers with Fc linkers, forming a random solid solution. During OER, the defects in Ni-BDC:Fc allow long-range molecule/electron transfer.

catalysts, of state-of-the-art 3d transition metal catalysts,[15−17] are much lower compared to those in biological systems.[18,19] For example, the TOF of Co-BDC-Fc-NF, which includes defects in the structure aimed at improving activity, is about 0.034 s^{-1}; and this work focuses solely on activity without exploring stability or conducting a more in-depth mechanistic study.[20] Furthermore, NiFe-LDH, which serves as a model alkaline OER catalyst, exhibits high activity but phase segregates due to the irreversible redeposition of dissolved Fe and Ni cations during the OER, resulting in fast current decay over time, especially at high current densities.[21] Metal−organic electrocatalysts (MOEs), constructed from metal nodes and organic linkers, offer the opportunity to tune activity−stability by varying the metal centers and linkers, thereby altering the local active environments.[22−25] For instance, Yuan et al. have synthesized tunable MOEs by using different linkers from L1 (terephthalic acid) to L4 (azobenzene-4,4′-dicarboxylic acid), where Fe/$Ni_2(OH)_2$(L4)/C has a TOF of 0.30 s^{-1} at 1.53 V_{RHE}.[26] Following work by Zheng et al. has revealed that although the L4 linker shows better stability than the L1 linker, the TOF of Fe/$Ni_2(OH)_2$(L4) is lower than that of Fe/$Ni_2(OH)_2$(L1), further demonstrating the typical problem and trade-off between activity and stability.[27−29]

Defect engineering is a potential way to break this trade-off, as previous works[30−32] have shown that ligand vacancies in MOEs can lower the energy barrier for *OH deprotonation,[33] while defects can enhance the stability of metal−organic materials.[34] Therefore, optimal defects are likely to not only enhance the intrinsic activity but also increase the utilization of internal bulk sites via unsaturated metal sites. In addition, these defects can help preserve the local active environments by acting as a buffer for structure, thereby maintaining long-range molecular and electron transport to improve the catalyst activity and stability.

As such, we created defects in Ni-based MOEs through mixing linkers of 1,4-benzenedicarboxylic acid (BDC) and ferrocenecarboxylic acid (Fc) within the structure. When the nominal ratio of BDC and Fc is 5:1 during synthesis, the Ni-BDC:Fc_5:1 exhibited higher activity−stability compared to other ratios and pure Ni-BDC. The TOF of Ni-BDC:Fc_5:1 was measured to be ∼0.75 O_2 s^{-1} at 1.53 V_{RHE}, whereas an overpotential of 380 mV is required to reach a current density of 500 mA cm_{geo}^{-2}. Furthermore, the cyclic voltammetry (CV) curves of Ni-BDC:Fc_5:1 showed negligible changes over 500 cycles. To demonstrate the increased structural stability during the OER, in situ surface-enhanced Raman spectroscopy (SERS) revealed the existence of linkers within the structure of Ni-BDC:Fc_5:1 at 1.7 V_{RHE}, while the linkers in Ni-BDC are lost after 1.30 V_{RHE}. Furthermore, surface-enhanced infrared adsorption spectroscopy (SEIRAS) indicated more isolated water/OH^- in Ni-BDC:Fc_5:1, which can facilitate easier mass transport of reactants and products to and from the active sites, respectively. Isotope-labeled electrochemical mass spectrometry (EC-MS) also showed that Ni-BDC:Fc_5:1 has more stable local active environments. Theoretical calculations indicated that unsaturated Ni sites have a lower thermodynamic barrier for the rate-determining step (RDS) compared to Ni-BDC. Benefiting from the properties of the material, an AEMWE constructed using Ni-BDC:Fc_5:1 as the OER catalyst can achieve a current density of 1 A cm^{-2} with a cell voltage of ∼1.73 V_{cell} for over 120 h, demonstrating the promising potential of this material for practical hydrogen production.

RESULTS AND DISCUSSION

Defects Design and Characterization. The defects within the Ni-based MOE structure were realized by mixing different proportions of BDC and Fc linkers during the synthesis, as shown in Figure 1. In the case of pure BDC as the linker (Ni-BDC), in a perfect crystal, each Ni site is fully saturated with six Ni−O bonds connected to either the carboxylate group of the linkers or the terminal −OH groups. However, since Fc has only one carboxyl functional group but

https://doi.org/10.1021/jacs.5c06156
J. Am. Chem. Soc. 2025, 147, 29838−29851

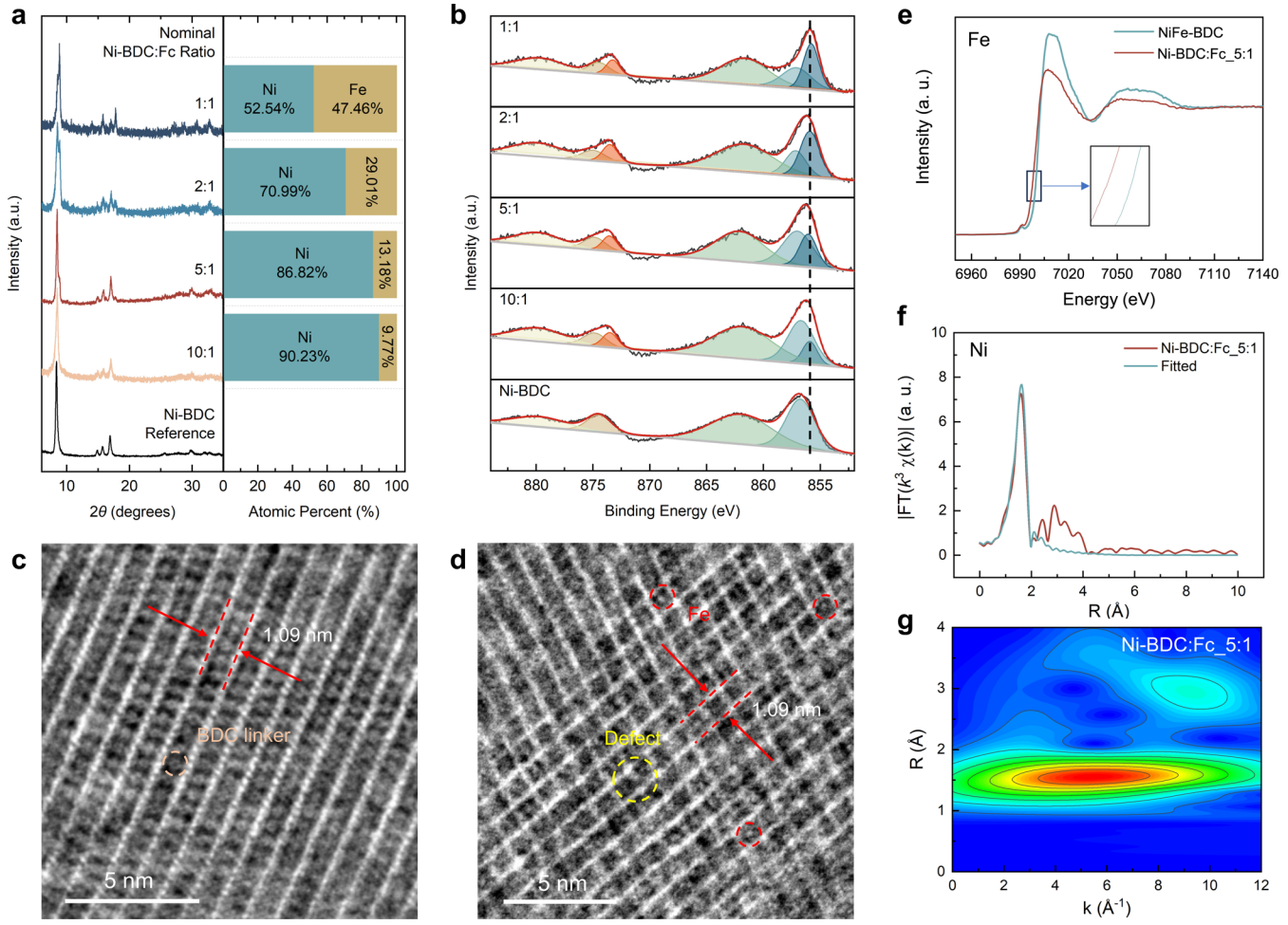

Figure 2. Material characterization of Ni-BDC and Ni-BDC:Fc MOEs. (a) XRD patterns and ICP-OES elemental analysis (relative Ni and Fe atomic percent). (b) Ni 2p XPS spectra of Ni-BDC:Fc_10:1, Ni-BDC:Fc_5:1, Ni-BDC:Fc_2:1, and Ni-BDC:Fc_1:1. Ni-BDC are used as a reference. (c,d) iDPC-STEM image of (c) Ni-BDC and (d) Ni-BDC:Fc_5:1. (e) Fe K-edge of XANES spectra of Ni-BDC:Fc_5:1 and NiFe-BDC. (f) Ni K edge Fourier transformed EXAFS spectrum and fitted curve of Ni-BDC:Fc_5:1. (g) Wavelet transform of Ni-BDC:Fc_5:1.

two five-membered rings sandwiching an Fe atom, when coordinated with the Ni−OH layers, a single Fc linker occupies the space of two BDC ligands, thus potentially creating three unsaturated Ni sites. The ratios of BDC to Fc during synthesis are selected as 10:1, 5:1, 2:1, and 1:1, which were hypothesized to allow for controlling the concentration of defects within the structure. The resulting materials are named Ni-BDC:Fc_10:1, Ni-BDC:Fc_5:1, Ni-BDC:Fc_2:1, and Ni-BDC:Fc_1:1, respectively. In this design, any OH^- attack on fully coordinated Ni sites in Ni-BDC would disrupt Ni−ligand bonds, leading to structural collapse. In contrast, Ni-BDC:Fc features unsaturated Ni sites with higher activity, where OH^- can adsorb on these sites without breaking Ni−ligand bonds, simultaneously improving the activity and stability.

X-ray diffraction (XRD) was employed to ensure that the use of additional linkers did not alter the crystal structures of the materials. The XRD pattern of pure Ni-BDC agrees with previously reported results.[26,27] The MOEs with mixed linkers showed nearly the same XRD patterns as Ni-BDC (Figure 2a), except that the peak around 8° (001) exhibits a small peak to the right of the main peak that gradually intensifies as the Fc content increases (Figure S1). As the Fc linker is slightly shorter than the BDC linker, inclusion of Fc within the structure should decrease the (001) spacing of the MOE, making the XRD reflection shift to a higher 2θ. As such, the emerging peak to the right of the main peak around 8° suggests that Fc was successfully incorporated into the layered MOE structure. Furthermore, as only Ni salts were used during the synthesis, the detection of Fe serves as an indicator of the presence of the Fc ligand within the structure. Inductively coupled plasma-optical emission spectrometry (ICP-OES) was used to determine the relative Ni and Fe contents of the materials synthesized with different linker ratios. As expected, the relative amounts of Fe exhibited a monotonically increasing trend with the proportion of Fc precursors added during the synthesis (Figure 2a), further supporting that varying degrees of linker substitution were achieved.

The purpose of using mixed ligands is to introduce defects (i.e., unsaturated Ni sites) within the MOE structure. High-resolution XPS of Ni 2p was therefore used to probe the different Ni identities within the structure, as displayed in Figure 2b. While only one peak at 856.8 eV was fitted for the Ni $2p_{2/3}$ region in Ni-BDC, the Ni $2p_{2/3}$ region of the mixed linker MOEs can be deconvoluted to two peaks centered at 857.0 and 856.1 eV, which are ascribed to the saturated Ni sites and unsaturated Ni sites, respectively. Also, the entire Ni $2p_{2/3}$ peak shifted to lower binding energy by about 0.8 eV (Figure S2) from Ni-BDC (856.7 eV) to Ni-BDC:Fc_1:1

https://doi.org/10.1021/jacs.5c06156
J. Am. Chem. Soc. 2025, 147, 29838−29851

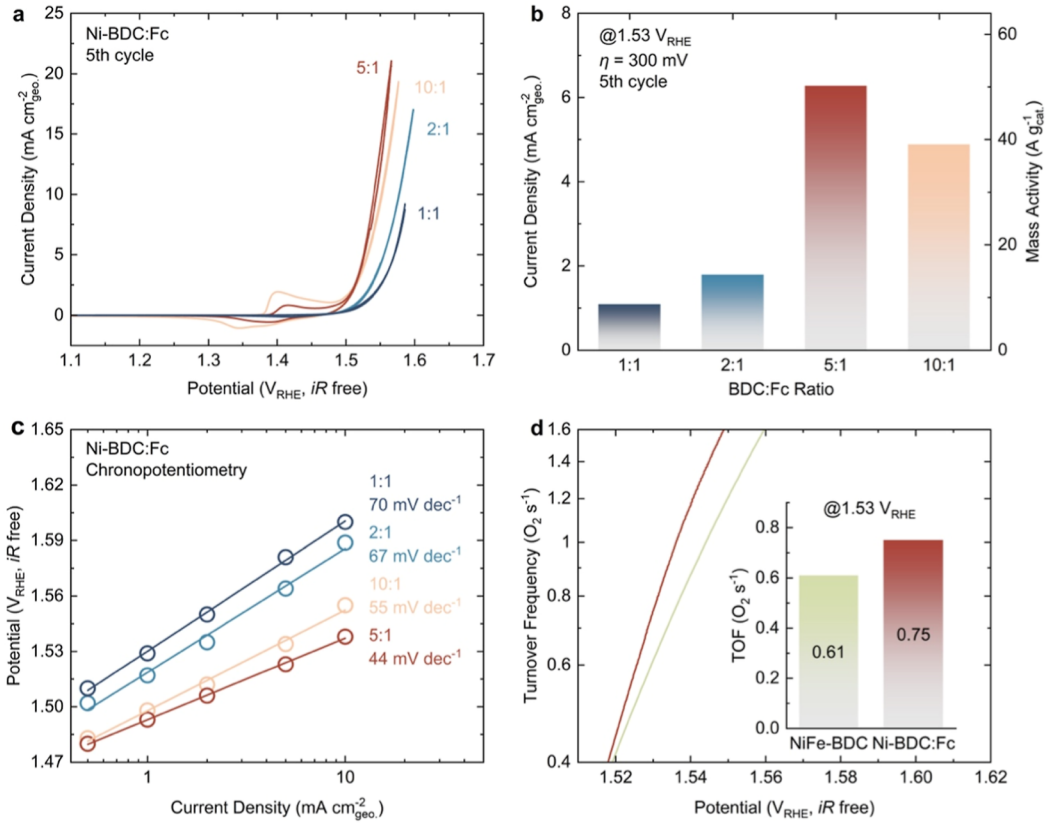

Figure 3. OER activity of Ni-BDC:Fc. (a) 5th CV cycle of Ni-BDC:Fc_10:1, Ni-BDC:Fc_5:1, Ni-BDC:Fc_2:1, and Ni-BDC:Fc_1:1 with scan rate of 10 mV s^{-1} at 1600 rpm in O_2 saturated 0.1 M KOH electrolyte in a three-electrode system. (b) Current density and mass activity at 1.53 V_{RHE} of different BDC/Fc ratio MOEs for OER. (c) Tafel plot of OER activity measured from chronopotentiometry (CP) measurements with the fitted Tafel slopes. (d) Turnover frequency (TOF) of Ni:BDC:Fc_5:1 and NiFe-BDC as a function of potential. Insert highlights the TOF at 1.53 V_{RHE}. The catalyst loading is 125 μg cm^{-2} on a 0.196 cm^2 glassy carbon disk. A Hg/HgO reference and carbon rod counter electrodes were used. 100% *iR* correction was used.

(855.9 eV) as more Fc linker was included. NiFe-BDC was synthesized with the same nominal ratio of Ni/Fe as in Ni-BDC:Fc_5:1 to compare the effects of Fe. The Fe (which is found within the M−OH layers) peak in NiFe-BDC, showed higher binding energy than the Fe in the mixed linker MOEs. The Fe peaks were also shifted to lower energy as more Fc linkers were incorporated into the MOEs (Figure S3). Moreover, the Ni 2p regions of NiFe-BDC also fit best with one peak, like Ni-BDC, suggesting that the peak changes in the mixed linker Ni-BDC:Fc_5:1 are not attributed to Fe incorporated into the M−OH layers but are due to the difference in coordination environments (Figure S4). The existence of defects in Ni-BDC:Fc_5:1 is further supported by more obvious spikes in the peak electron-paramagnetic resonance (EPR) spectra with $g = 2$ (Figure S5), which is usually associated with unpaired electrons.

In order to directly observe the mixed linkers and defects, integrated differential phase contrast (iDPC) via scanning transmission electron microscopy (STEM) was used to obtain atomic-resolution images of the MOEs. The observed lattice spacings of Ni-BDC and Ni-BDC:Fc 5:1 match well with the length of both the BDC and Fc linkers (∼1.09 nm) (Figures 2c,d, S6, and S7a). In the image, between two columns with higher relative intensity (Ni−OH layers), the six-membered ring of BDC can be clearly observed for Ni-BDC (Figure 2c, circled). However, because of the many defects in Ni-BDC:Fc_5:1, the structure of the Fc linker cannot be observed as clearly as in Ni-BDC (Figures 2d and S7b). Nevertheless, some features captured through iDPC still support the idea that defects were included in the structure. For example, the observation of bright atoms between Ni columns (Figure 2d, circled in red) agrees with the location of Fe in the Fc linker. In addition, a relatively blank area (Figure 2d, circled in yellow) near the Ni suggests that defects exist in Ni-BDC:Fc_5:1, which is consistent with unsaturated Ni sites. We also examined other sheets to show that the defects were included homogeneously within the material (Figure S8), all of which support that defects were included in NiBDC:Fc_5:1. To further reveal the difference between Ni-BDC and Ni-BDC:Fc_5:1, Brunauer−Emmett−Teller (BET) and Barrett−Joyner−Halenda (BJH) measurements were carried out. While the Ni-BDC exhibited an adsorption−desorption curve characteristic of a mesoporous structure, the rapid increase observed in Ni-BDC:Fc_5:1 at low relative pressures indicates the presence of more micropores in its structure (Figure S9). Moreover, the pore distribution from BJH analysis showed that Ni-BDC:Fc_5:1 contains significant pore volume below 2 nm, suggesting the presence of abundant defects in Ni-BDC:Fc_5:1 (Figure S10) as the interlayer spacing is ∼1 nm.

To understand the local structure of Ni and Fe in the synthesized samples, we performed Ni and Fe K-edge X-ray absorption spectroscopy. The Fe K-edge X-ray absorption near-edge structure (XANES) spectrum of Ni-BDC:Fc_5:1 exhibits a lower absorption edge compared to that of NiFe-

https://doi.org/10.1021/jacs.5c06156
J. Am. Chem. Soc. 2025, 147, 29838−29851

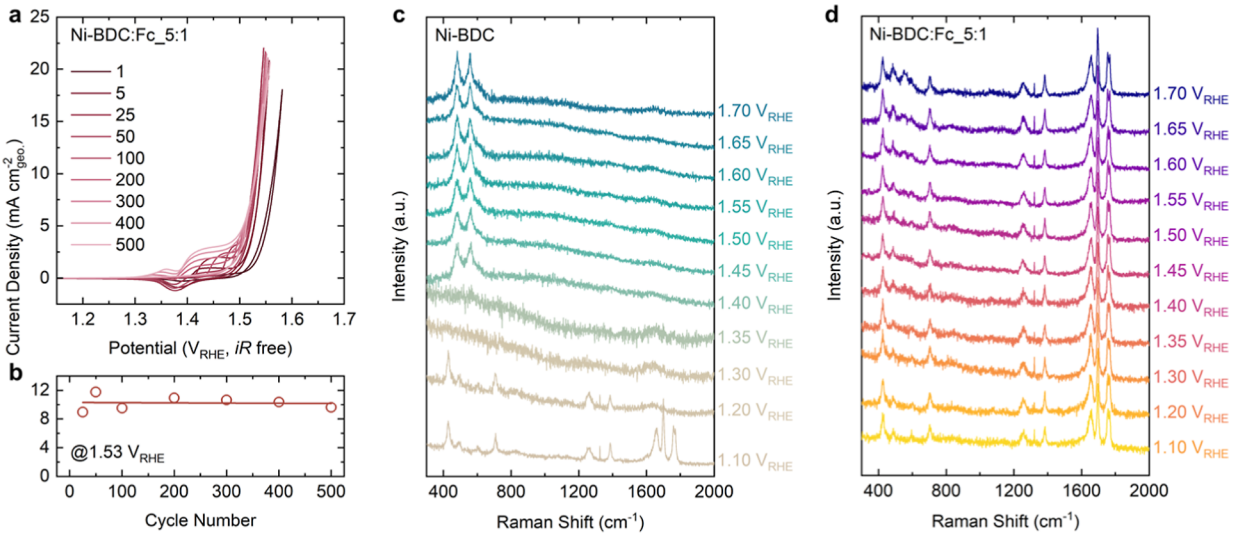

Figure 4. Stability and different in situ spectroscopy analysis of Ni-BDC:Fc_5:1. (a) 500 CV cycles and (b) current density at 1.53 V_{RHE} of Ni-BDC:Fc_5:1 at 1600 rpm with a scan rate of 10 mV s^{-1} in O_2-saturated 0.1 M KOH. Catalyst loading: 125 $\mu g\ cm_{geo}^{-2}$ on 0.196 cm^2 GC disk. (c-d) In situ Raman spectroscopy of (c) Ni-BDC and (d) Ni-BDC:Fc_5:1 from 1.1 V_{RHE} to 1.70 V_{RHE} in 0.1 M KOH.

BDC (Figure 2e), indicating a lower oxidation state of Fe in Ni-BDC:Fc_5:1, which is consistent with previous XPS results. The lower white line intensity in the Fe K-edge XANES of Ni-BDC:Fc_5:1 can be attributed to differences in the local coordination environment (π-conjugated cyclopentadienyl ligands in Fc) and the electronic structure around the Fe centers. The fitted coordinated number of Fe in NiFe-BDC and Ni-BDC:Fc_5:1 is 6.4 and 10.7 (Figure S11 and Table S1), respectively, further supporting that Fe in Ni-BDC:Fc_5:1 is not substituted in the M−OH sheets but rather originates from the incorporated Fc linker (since Fc has two 5 membered rings coordinated to an iron atom). The Ni K-edge XANES spectra of Ni-BDC, Ni-BDC:Fc_5:1, and NiFe-BDC show no significant differences, indicating similar overall crystal structures (Figure S12a). However, fitting the Fourier-transformed extended X-ray absorption fine structure (EXAFS) data (Figures 2f and S12b) reveals that the average coordination number of Ni decreases from 6.3 in Ni-BDC to 5.8 in Ni-BDC:Fc_5:1 (Table S2), suggesting the presence of unsaturated Ni sites in the latter due to defect formation. The WT analysis for Ni-BDC and Ni-BDC:Fc_5:1 both shows the strongest intensity at around 5 $Å^{-1}$ and 1.5 Å in *R*-space, corresponding to the scattering from oxygen atoms surrounding the central Ni atom (Figures 2g and S12c).

Defects Effect on OER Activity−Stability. According to our hypothesis, a moderate level of defects is expected to achieve optimal activity, as too few defects fail to provide sufficient unsaturated sites, while excessive defects may hinder electron transfer. As the first few cycles of CV can be affected by factors that obscure the measuring of intrinsic activity, such as poor wetting, the polarization curve of the fifth cycle was used to compare the activity (Figure 3a). A volcano-trend for the activity as a function of Fc content was observed for the mixed linker MOEs, with Ni-BDC:Fc_5:1 exhibiting the highest activity among the four mixed linker catalysts and pure Ni-BDC (Figure S13). As shown in Figure 3b, at 1.53 V_{RHE} (overpotential η = 300 mV), the current density of Ni-BDC:Fc_5:1 was 6.28 mA cm^{-2}, which is about 40 times higher than that of Ni-BDC at the same potential (0.16 mA cm^{-2}). Meanwhile, the mass activity of Ni-BDC:Fc_5:1 at 1.53 V_{RHE} was measured to be 50.2 A g^{-1}_{cat} (Figure 3b, right axis), which is about 6× higher than commercial IrO_2 nanoparticles with the same mass loading (Figure S14). To further evaluate the differences in intrinsic activity among the MOEs, the electrochemically active surface areas (ECSAs) of the catalysts were measured using CV in a non-Faradaic region (Figure S15), and comparable values were found across all samples. ECSA-normalized OER activities (Figure S16) still follow the same trend as the geometric and mass activities, with Ni-BDC:Fc_5:1 showing the highest activity, confirming that the enhanced performance mainly arises from defect engineering rather than ECSA differences.

Figure 3c shows the estimated Tafel slope measured by using chronopotentiometry of the mixed linker catalysts (Figure S17). The Ni-BDC:Fc_5:1 showed the lowest Tafel slope of 44 mV dec^{-1} compared to those of Ni-BDC:Fc_10:1 (55 mV dec^{-1}), Ni-BDC:Fc_2:1 (67 mV dec^{-1}), and Ni-BDC:Fc_1:1 (70 mV dec^{-1}). The Tafel slope of Ni-BDC:Fc_5:1 suggests that the RDS is likely the *O to *OOH transition.[35] Although other catalysts with different BDC/Fc ratios exhibit slightly higher Tafel slopes, this does not necessarily imply a change in reaction mechanism, as their active site environments remain similar, but the Tafel slope could be a function of applied overpotentials.[36] The observed differences in Tafel slopes are likely influenced by multiple factors. From 10:1 to 5:1, increased defect density facilitates OH adsorption, resulting in a reduced Tafel slope. However, further increasing defects (e.g., in the 1:1 sample) may alter the intermediate coverage or affect the charge transfer coefficient, leading to a modest increase. Moreover, the TOF of OER was calculated at different potentials using the Ni^{2+}/Ni^{3+} redox peak to quantify the number of electrochemically active Ni sites, as shown in Figure 3d. NiFe-BDC is taken as a benchmark because it exhibits a higher TOF than most other OER catalysts and has nearly the same structure as Ni-BDC:Fc_5:1 at 1.53 V_{RHE}. The TOF of Ni-BDC:Fc 5:1 was calculated to be 0.75 O_2 s^{-1} as a lower bound (1.28 O_2 s^{-1} for the upper bound), while the lower bound TOF of NiFe-BDC was 0.61 O_2 s^{-1} at the same potential, exceeding the TOF for a majority of reported catalysts (Table S3).

https://doi.org/10.1021/jacs.5c06156
J. Am. Chem. Soc. 2025, 147, 29838−29851

To more accurately reflect that the differences in OER activity are caused by defects rather than stemming from different Fe contents, NiFe-BDC with varying Ni/Fe ratios was synthesized based on the elemental analysis results of the mixed linker MOEs and used for comparison. For all catalysts measured, Ni-BDC/Fc showed enhanced OER activity compared to the corresponding NiFe-BDC with nominally similar Ni/Fe ratios, suggesting that the purposeful inclusion of defects is the main cause of the observed enhanced OER activity (Figure S18). Furthermore, upon closer inspection of the Ni^{2+}/Ni^{3+} redox peaks, Ni-BDC/Fc exhibits larger redox peaks, indicating more electrochemically active sites compared to NiFe-BDC. Considering the proposed structure of the defect MOE, measuring more electrochemically active Ni sites in Ni-BDC/Fc compared to the defect-free material is expected, as the unsaturated sites in the MOE can directly serve as active sites for OER. Additionally, the Ni^{2+}/Ni^{3+} oxidation peak in Ni-BDC:Fc_5:1 could be fitted into two distinct peaks, likely representing two different types of Ni sites, which is consistent with the intended MOE design and XPS characterization.

After investigating the effect of defects on activity, we shifted our focus to evaluating the electrochemical stability of the materials. It is well-known that many catalysts, particularly MOEs,[37] suffer from rapid performance degradation during the OER due to structural transformations. We hypothesize that too few defects may lead to structural collapse during the OER due to the inaccessibility of redox-active metal centers, while an excessive number of defects can render the initial structure insufficiently rigid and inherently unstable. To verify this hypothesis, the Ni-BDC/Fc catalysts were subjected to 500 CV cycles between 1.1 and 1.75 V_{RHE} in O_2 saturated 0.1 M KOH at 10 mV s^{-1} (~18 h of continuous cycling) to monitor their electrochemical evolution. The 500 CV curves of Ni-BDC:Fc_5:1 largely overlapped, while the OER polarization curves remained nearly unchanged, demonstrating exceptionally high stability (Figure 4a). However, Ni-BDC:Fc_10:1 initially exhibited an increase in activity followed by a slight decay (Figure S19) beyond 400 cycles, which can be ascribed to too many saturated sites in the pristine Ni-BDC:Fc_10:1 causing structural disruption and gradually transforming into $NiOOH_{2-x}$-like phases upon cycling.[29] Furthermore, the OER activities of Ni-BDC:Fc_2:1 and 1:1 peaked at the beginning and then steadily declined (Figure S20) during the cycling. The moderate level of defects in Ni-BDC:Fc_5:1 may have acted as a buffer against structural changes. While structural transformation might eventually occur, it did not lead to any significant activity decay (Figure 4b).

To directly probe the structural changes during the OER process, in situ SERS was performed on Ni-BDC:Fc_5:1 and Ni-BDC under different applied potentials (from 1.1 to 1.7 V_{RHE}) in a 0.1 M KOH electrolyte. At the initial potential (1.1 V_{RHE}), both Ni-BDC/Fc and Ni-BDC exhibited similar features (400−800 cm^{-1}, 1200−1400 cm^{-1}, and 1600−1800 cm^{-1}), which are consistent with them having similar structures. As the potential was gradually increased, in Ni-BDC (Figure 4c), the peaks located at 1600−1800 cm^{-1} disappeared at 1.2 V_{RHE}, while other peaks remained, indicating that Ni-BDC had already begun undergoing a structural transformation, even before the onset of the OER potentials. At applied potentials of 1.30 and 1.35 V_{RHE}, all peaks of Ni-BDC irreversibly disappeared, suggesting that the linkers leached out from the MOE structure. The loss of all linkers at precisely 1.30 V_{RHE} is consistent with our previous work that showed the oxidation process of Ni^{2+} to Ni^{3+} facilitates the structural transition to $NiOOH_{2-x}$-like phases, highlighting the instability of the Ni-BDC structure.[27] As the potential was further increased beyond 1.40 V_{RHE}, two peaks appeared and gradually intensified at 481.4 cm^{-1} and 559.1 cm^{-1}, corresponding to the Ni−O vibrational modes parallel (E_g bending (δ)) and perpendicular (A_{1g} stretching (ν)) to the $NiOOH_{2-x}$-like phases, respectively.[38] Although Ni-BDC is highly unstable, the spectra of Ni-BDC:Fc_5:1 exhibited unexpectedly little change as a function of the potential (Figure 4d) in comparison. From 1.1 to 1.70 V_{RHE}, all peaks present in the pristine material remained with little decrease in intensity, suggesting that the linkers remained largely in the MOE structure and implying the increased stability of the MOE structure. Moreover, unlike Ni-BDC, which showed Ni−O vibrational bands found in $NiOOH_{2-x}$-like phases at 1.40 V_{RHE}, Ni-BDC:Fc_5:1 did not show these two peaks until the potential increased to 1.60 V_{RHE}. In fact, only a relatively broad band appeared around 559 cm^{-1}, which suggests that the unsaturated Ni sites can directly act as the OER active sites. At 1.70 V_{RHE}, the δ and ν stretching modes, located at 483.9 cm^{-1} and 551.9 cm^{-1}, respectively, emerged while the other linker peaks still remained, suggesting that although the Ni sites underwent oxidation and some structural transformation, the defects effectively buffered these changes and significantly increased stability by deterring the loss of linkers.

In the evaluation of the structural stability of the catalyst, it is important to consider not only the robustness of the organic linker but also the chemical stability of the Ni centers themselves. Ni-based materials tend to convert into $Ni(OH)_2$ or NiOOH under alkaline conditions from OH^- attack. In Ni-BDC, the Ni−ligand bonds are more prone to be disrupted by OH^-, leading to structure collapse and formation of $Ni(OH)_2$. In contrast, Ni-BDC:Fc_5:1 exhibits enhanced structural flexibility due to moderate defect levels, which helps maintain the resilience of Ni−ligand coordination during the OER. However, excessive defects, as in Ni-BDC:Fc_1:1, reduce framework rigidity and increase the freedom of Ni centers, resulting in $Ni(OH)_2$ formation and performance decay. Therefore, the Ni stability is a relevant factor in catalyst durability and is affected by the BDC/Fc ratio.

To further explore how long Ni-BDC:Fc_5:1 can remain stable under harsh OER conditions, we held the potential at 1.6 V_{RHE} and monitored the evolution of the Raman spectra over time (Figure S21). Although the peaks present in the pristine materials were eventually replaced by peaks corresponding to the Ni−O δ and ν modes, the measured electrochemistry data appeared to remain stable during the spectroscopy measurement, which suggests that even though structural transformation is inevitable, defects or local active environments could be preserved during the transition, allowing the stability of the OER activity to remain largely unaffected. The possible preservation of defects post-transformation is supported in the I_δ/I_ν intensity ratio. After the complete transformation, the relative I_δ/I_ν intensity ratio of Ni-BDC:Fc_5:1 was lower than that of Ni-BDC, indicating that Ni-BDC:Fc_5:1 retained more vacancies or had a lower Ni-oxidation state post-transition (Figure S22).[39] This aligns with previous expectations, as the unsaturated Ni sites inherently possess greater disorder and a lower oxidation state, which is beneficial for OER performance.[40]

https://doi.org/10.1021/jacs.5c06156
J. Am. Chem. Soc. 2025, 147, 29838−29851

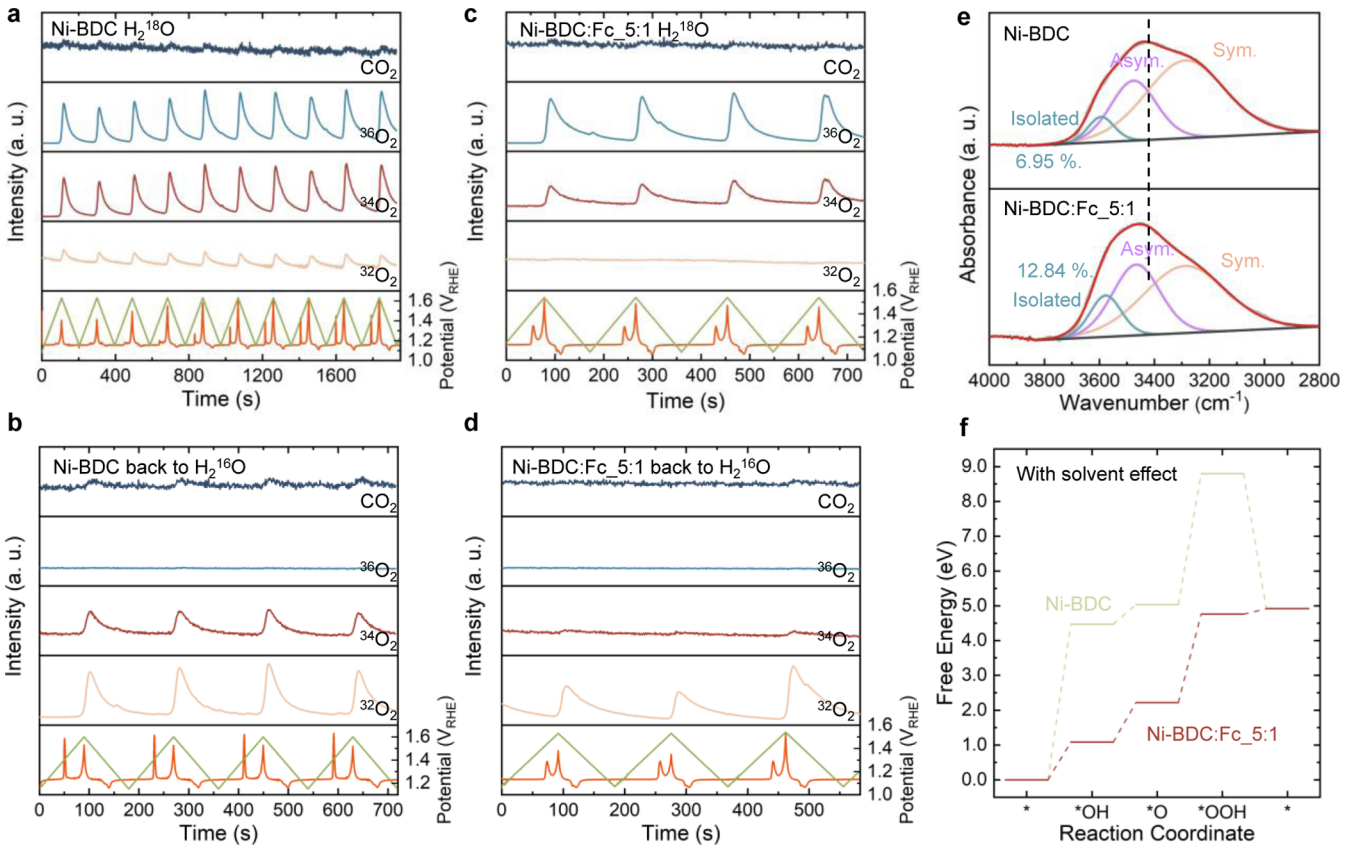

Figure 5. Understanding the role of defects on the electrochemical activity−stability. (a−d) CV scans and time-dependent MS signal of different species ($^{32}O_2$, $^{34}O_2$, $^{36}O_2$, and $^{44}CO_2$) with 0.1 M KOH in isotope labeled $H_2{}^{18}O$ of (a) Ni-BDC and (c) Ni-BDC:Fc_5:1. After that, the electrolyte was changed back to normal 0.1 M KOH in $H_2{}^{16}O$ for (b) Ni-BDC and (d) Ni-BDC:Fc_5:1. The green line in (a−d) represents the potential change and the orange line represents current change along time. (e) The deconvolution of the OH stretching peak of Ni-BDC and Ni-BDC:Fc_5:1 acquired in 1 M KOH electrolyte under open-circuit potential by SEIRAS. (f) Free energy diagram of OER with solvent effect following the absorbate-mediated evolution pathway for Ni-BDC:Fc_5:1 and Ni-BDC at 0 V_{RHE}.

Mechanism of Defects Enhancing Activity−Stability. To demonstrate that the purposeful inclusion of defects increases the electrochemical stability of the MOEs, EC-MS in isotope-labeled oxygen-18 (^{18}O) electrolyte was used to understand the OER mechanism and materials degradation. 0.1 M KOH in $H_2{}^{18}O$ was used as the electrolyte, making the potential products include O_2 at m/z = 32, 34, or 36, noted as $^{32}O_2$, $^{34}O_2$, and $^{36}O_2$, respectively. CO_2 at m/z = 44 was also measured due to the presence of −COOH functional groups on the linkers or potential carbon oxidation. During CV scans, the redox peak of Ni-BDC intensified rapidly after 10 cycles, whereas that of Ni-BDC:Fc_5:1 remained relatively stable, consistent with our previous electrochemical measurements. For the reaction products, both Ni-BDC and Ni-BDC:Fc_5:1 exhibited clear signals of $^{36}O_2$. However, for Ni-BDC, $^{32}O_2$ was also observed (Figure 5a), which was nearly undetectable for Ni-BDC:Fc_5:1 (Figure 5c). Additionally, Ni-BDC showed relatively stronger signals for the carbon monoxide-based molecules CO_2 and $^{34}O_2$. Taken together, these results suggest that lattice oxygen is involved in the reaction or oxygen exchange with the electrolyte during the OER of Ni-BDC. In either case, oxygen evolution from the MOE lattice highlights the structural instability of Ni-BDC during the reaction. When the electrolyte was switched back to 0.1 M KOH in $H_2{}^{16}O$ with the same electrode, the signal for $^{32}O_2$ was observed, while the signal for $^{36}O_2$ nearly disappeared for both catalysts. However, similar to previous observations, Ni-BDC exhibited stronger relative signals for $^{34}O_2$ and CO_2 (Figure 5b), indicating that a portion of the isotope-labeled oxygen had previously exchanged into the Ni-BDC structure. In contrast, for Ni-BDC:Fc_5:1, a minimal amount of $^{34}O_2$ was detected (Figure 5d), reflecting its ability to effectively buffer structural changes due to the presence of defects. Coupled with the in situ SERS showing preservation of the MOE local structure even at elevated potentials, the defects may help preserve the local structure of the MOE by preventing significant lattice exchange of oxygen in the MOE structure with the electrolyte during the OER, even if there is long-range order degradation. As previous studies have shown that oxygen lattice exchange can lead to significant surface amorphization during OER,[41,42] the unsaturated sites within the MOE could help stabilize the material, as they could act as easily accessible OER active sites, which prevent the need for lattice oxygen exchange and maintain local short-range order during the reaction for molecular and electron transport.

As the BJH analysis showed a significant amount of porosity <2 nm in diameter, we also hypothesized that the defects allow for a significant number of internal sites to be electrochemically accessible and active for OER. Therefore, in situ SEIRAS was employed to probe the interfacial water structure of Ni-BDC and Ni-BDC:Fc_5:1. The MOE immersed in DI water was first measured to observe the interfacial water structure near the MOEs without an applied potential. In the range of 1000 cm^{-1}−1700 cm^{-1}, the infrared signals were primarily

https://doi.org/10.1021/jacs.5c06156
J. Am. Chem. Soc. 2025, 147, 29838−29851

attributed to C−O and C═C vibrations. The main signals of interest were observed in the range of 3000 cm^{-1}−3700 cm^{-1}, characteristic of O−H vibrations. The O−H peak of Ni-BDC:Fc_5:1 exhibited a slight shift to higher wavenumbers (Figure S23), suggesting that Ni-BDC:Fc_5:1 might contain more isolated water molecules. Still under open-circuit potential, using the same electrode but with a 1 M KOH electrolyte exacerbated the relative blue shift of the O−H peak for Ni-BDC:Fc_5:1 compared to that for Ni-BDC (Figure S24). The large peak between 3000 and 3700 cm^{-1} was deconvoluted to three peaks corresponding to isolated water or OH^- at 3570−3600 cm^{-1}, asymmetric H-bonded water at 3450−3480 cm^{-1}, and symmetric H-bonded water at 3270−3300 cm^{-1} (Figure 5e) based on previous reports.[43] Ni-BDC, with fewer defects, showed a higher proportion of asymmetric and symmetric H-bonded water, which is more indicative of bulk water near the external surface and consistent with the lack of internal porosity observed in the BJH analysis. However, we found that there was nearly double the relative amount of isolated water/OH^- in the defect MOE (12.84%) compared to the pure BDC (6.95%) MOE (Figures 5e and S25), which we ascribe to the higher number of defects and microporous structures in Ni-BDC:Fc_5:1. Furthermore, in situ potential-dependent IR results (Figure S26) showed that the peak position of the O−H bond gradually shifts to lower wavenumbers as the potential increases. For Ni-BDC, a distinct shift occurs after 1.35 V, indicating a significant decrease in the amount of isolated water/OH^- within the structure. However, this shift for Ni-BDC:Fc_5:1 appears after 1.40 V, further confirming the presence of more isolated water/OH^- in Ni-BDC:Fc_5:1 as indicated by previous results. Contact angle measurements were performed to exclude the effect of the Fc linker for the water/OH^- interfacial structure. Compared to Ni-BDC, which is already hydrophobic due to the aromatic BDC ligand, Ni-BDC:Fc_5:1 showed a larger contact angle (Figure S27), attributed to the more hydrophobic ferrocene moiety and fewer $-COO^-$ groups. Considering only hydrophobicity without confinement, a more hydrophobic interface would typically result in more water clustering at the interface due to relatively weaker interface−water interactions than water−water interactions compared to a hydrophilic interface. Thus, the higher water/OH^- retention in Ni-BDC:Fc_5:1 after soaking is not due to the Fc linker but rather to increased internal porosity resulting from defects. We hypothesize that these defects created internal porosity with exposed unsaturated Ni sites that can effectively adsorb OH^- or water molecules, isolating them from the bulk water structure. Therefore, the internal porosity of Ni-BDC:Fc_5:1 should be electrochemically accessible and active, where the defects could have facilitated the long-range shuttling of OH^- to the internal Ni sites for OER. This idea is supported by previous studies that have shown that defects in Ni-based MOEs can increase OH^- conductivity compared to the pristine state due to increased porosity and hydrophilicity of the Ni sites.[44] To confirm the higher OH^- conductivity in our defect MOE, we used electrochemical impedance spectroscopy (EIS). The higher measured OH^- conductivity of Ni-BDC:Fc_5:1 (2.06×10^{-6} S/cm) compared to that of Ni-BDC (7.69×10^{-7} S/cm) further supports that the defects introduced via the Fc linker facilitated H_2O/OH^- transport (Figure S28).

To further understand the role of defects in the enhanced OER activity−stability of Ni-BDC:Fc_5:1, density functional theory (DFT) calculations were conducted. A structure as close as possible to the real MOE was used for the calculations rather than the simplified metal−organic ligand clusters commonly employed in some studies. In addition, the Fc linker was introduced such that the unsaturated Ni site is found within the bulk structure, reflecting that the internal pores of the MOE appeared to be active. The interatomic distances from the relaxed MOE structure further support the ability for internal OH^- conduction, as the distance between an unsaturated Ni^{2+} site and the nearest H on the Fc linker was measured to be 4.2 Å, which is over 1 Å larger than the kinetic diameter of water (~3 Å).[45] A smaller band gap was calculated for the Fc-included structure compared with that of Ni-BDC as some new electronic states were generated near the Fermi level (E_F), suggesting that Ni-BDC:Fc_5:1 is more electrically conductive (Figure S29). The 3d-Ni projected density of state (PDOS) of Ni active sites was further calculated. Unlike the relatively symmetric PDOS of Ni atoms in Ni-BDC, the peak above E_F disappears, and there are more electronic states below E_F in the spin-up configuration, likely indicating a lower oxidation state of Ni, which is consistent with our XPS and Raman results (Figure S30). DFT was also used to calculate the OER energetics on Ni-BDC and Ni-BDC:Fc MOEs following the adsorbate evolution mechanism (based on the lack of lattice exchange in the EC-MS experiments). As such, in Ni-BDC:Fc_5:1, unsaturated Ni sites were chosen as the active sites for comparison, while any atom can be selected as the active site in Ni-BDC as each Ni atom is fully coordinated (Figures S31 and S32). Without solvation effects, the RDS for Ni-BDC:Fc_5:1 is the *O to *OOH step (Figure S33), which is consistent with the experimentally measured Tafel slope of ~44 mV dec^{-1} as typically a Tafel slope in the range of 40 mV dec^{-1} suggests that the RDS involves the formation of peroxide (OOH) or peroxo (OO) intermediates.[46−48] In comparison, the OER on Ni-BDC shows a high thermodynamic barrier for both *OH and *OOH formation. The Tafel slope of ~65 mV dec^{-1} for Ni-BDC at low overpotential, likely suggesting mixed RDSs, and increases to ~118 mV dec^{-1} at high overpotential, reflecting the influence of potential and surface coverage (Figure S34). When solvation effects are included, the first step ($* + OH^- \rightarrow *OH$) becomes the RDS for the OER on Ni-BDC due to the difficulty of OH^- adsorption on fully coordinated Ni sites and steric hindrance (Figure 5f). Moreover, DFT calculations are based on bulk Ni sites, while real samples also contain edge sites, where the RDS may differ. The experimentally observed Tafel slope thus reflects a combination of bulk and edge contributions of Ni-BDC. Nevertheless, regardless of solvation, the RDS energy gap for Ni-BDC:Fc_5:1 remains lower than that of Ni-BDC, supporting its superior activity. This smaller thermodynamic barrier implies that unsaturated Ni sites can significantly increase the rate of OER, as was observed experimentally.

Therefore, taking the data from the EC-MS, in situ SEIRAS, and DFT experiments all together, the defects within Ni-BDC:Fc_5:1 are multifunctional and modify the short- and long-range interactions of the MOE in ways that are all beneficial to the stability of the OER activity−stability. Specifically, the defects in the Ni-BDC:Fc_5:1created an environment that not only enhanced the intrinsic activity of the active sites for the OER but also preserved the local atomic environment of the active sites by inhibiting lattice oxygen exchange with the electrolyte to increase the longevity of these highly active sites. In addition, the defects created a porous network that activated sites within the material by facilitating

https://doi.org/10.1021/jacs.5c06156
J. Am. Chem. Soc. 2025, 147, 29838−29851

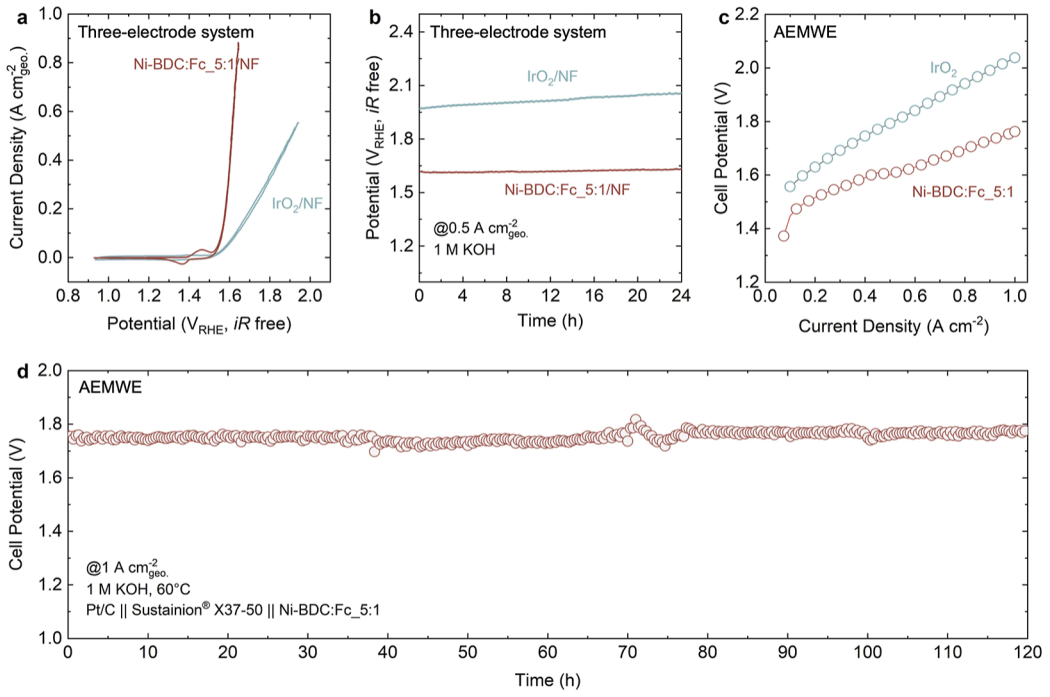

Figure 6. AEMWE performance of Ni-BDC:Fc_5:1. (a) CV curves at a scan rate of 10 mV s^{-1} and (b) stability tests of Ni-BDC:Fc_5:1/NF and IrO_2/NF in three-electrode system with 1 M KOH. 70% *iR* compensation was used. (c) Current−voltage polarization curves of the AEMWE cell with Ni-BDC:Fc_5:1 anode catalyst compared to commercial IrO_2 catalysts. (d) Galvanostatic measurement of the AEMWE device with 3 mg cm^{-2} Ni-BDC:Fc_5:1 as anode catalysts operated at 1 A cm^{-2} for 120 h. Test conditions: 1 mg cm^{-2} Pt/C (Tanaka Kikinzoku, 46 wt %) as cathode catalyst, Sustainion® X37−50 as the anion-exchange membrane. 1 M KOH was circulated through the anodic chamber. The entire setup was maintained at ∼60 °C.

long-range H_2O/OH^- conduction throughout the bulk material. Fundamentally, electrochemical reactions require the binding of reactants to active sites and the transfer of electrons. Therefore, the stability of the local structure ensures durability of the performance, which is highly valuable for practical applications.

AEMWE Performance. Based on the above analysis, the linker substitution strategy can greatly enhance the structure of a material to improve both the OER activity and stability, suggesting that Ni-BDC:Fc_5:1 could be utilized in practical water-splitting applications. In a three-electrode setup, instead of previous measurements using a low loading on rotating disk electrodes, nickel fiber (NF), commonly used as a gas diffusion layer in water splitting devices, was employed as the substrate to measure the OER activity. In an 1 M KOH electrolyte, the Ni-BDC:Fc_5:1 catalyst requires only an overpotential of 0.38 V to achieve a current density of 500 mA cm^{-2}, whereas commercial IrO_2, requires 0.67 V to reach the same current density (both with only 70% *iR* compensation), directly demonstrating the high OER activity of Ni-BDC:Fc_5:1 (Figure 6a). The estimated TOF of Ni-BDC:Fc_5:1/NF is 0.88 O_2 s^{-1} (lower bound, 1.50 O_2 s^{-1} for higher bound), higher than other reported catalysts in similar conditions (Table S3). Also, the stability of Ni-BDC:Fc_5:1 and IrO_2 was assessed under a constant current density of 500 mA cm_{geo}^{-2} for 24 h (Figure 6b), which showed that the potential for Ni-BDC:Fc_5:1 remains nearly constant after 24 h, while there was around a change of 0.2 V for IrO_2.

To demonstrate the feasibility of using defected MOEs as the OER catalysts in a zero-gap AEMWE device, membrane electrode assemblies with commercial Pt/C catalysts for the HER and Ni-BDC:Fc 5:1 catalyst for the OER were constructed to assess practical hydrogen production ability. An AEMWE with commercial IrO_2 as OER catalyst was also constructed for comparison. Figure 6c depicts the polarization curves of AEMWE devices (area: 2 cm × 2 cm) with Ni-BDC:Fc_5:1 and commercial IrO_2 anode catalysts at ∼60 °C in 1 M KOH electrolyte. The commercial IrO_2 required ∼2.03 V_{cell} to reach a current density of 1 A cm^{-2}, agreeing with previously reported results.[49] In contrast, the AEMWE with Ni-BDC:Fc_5:1 as the OER catalyst only needed ∼1.73 V_{cell} to reach 1 A cm^{-2}, in comparison, demonstrating that the higher kinetics of the OERs measured in a three-electrode setup were translated to the AEMWE device. Notably, such performance (∼1.73 V_{cell} @ 1 A cm^{-2}) already exceeds most reported AEMWE cell voltages (Table S4) and the 2026 target proposed by the Office of Energy Efficiency and Renewable Energy (EERE) in the US Department of Energy (1 A cm^{-2} @ 1.80 V).[50] Furthermore, the AEMWE demonstrated excellent performance even at higher current densities (Figure S35), requiring only 2.0 and 2.2 V_{cell} at current densities of 2 and 3 A cm^{-2}, respectively, further highlighting its promising potential for practical applications. To probe changes to the structural stability after AEMWE measurements, Raman spectra of the anode electrode were collected after high current densities (sweeps up to 3 A cm^{-2}) and constant current tests (1 A cm^{-2}) at three unique locations in the electrode. Two locations (Figure S36, spots 1 and 2) showed characteristic linker peaks and Ni−O vibrational peaks around 490−550 cm^{-1}. The Ni−O vibrations were higher in intensity for spot 1, suggesting spot 1 may have started structural transformation (Figure S36). However, the third spot only showed Ni−O peaks, indicating either a structural transformation of the MOEs under high current density or a possible detachment of the catalyst from

https://doi.org/10.1021/jacs.5c06156
J. Am. Chem. Soc. 2025, 147, 29838−29851

the Ni fiber, exposing the underlying Ni substrate. Nevertheless, compared to the rapid structural transformation observed for Ni-BDC, these results still indicate the superior structural and performance stability of Ni-BDC:Fc_5:1.

AEMWEs were also subjected to a constant current density of 1 A cm^{-2} to measure the stability of the device with different OER catalysts (Figure 6d). Similar to the result in the three-electrode setup, the AEMWE with IrO_2 showed a fast rate of voltage increase, going from 2.03 to 2.15 V_{cell} after only 18 h of testing (Figure S37). To enable a fair comparison, NiFe-LDHs (Ni/Fe 3:1), which are known as high-performance anode catalysts for AEMWE, were also synthesized following methods reported in literature[51] and tested under identical conditions. The polarization curve shows that NiFe-LDHs require a cell voltage of ∼1.81 V to reach 1 A cm^{-2}. Moreover, under constant current operation (1 A cm^{-2}), they exhibit no further activation and maintain a stable voltage of ∼1.84 V over 24 h (Figure S38). For Ni-BDC:Fc_5:1, the catalyst may have been further activated during the testing, as it reached a voltage of 1.71 V_{cell} for 1 A cm^{-2} for a portion of the measurements. The electrolyzer using Ni-BDC:Fc_5:1 as the OER catalyst was stably operated for over 120 h with negligible performance decay.

CONCLUSION

In summary, we successfully created varying degrees of defects in Ni-based MOEs by utilizing a linker substitution strategy. Ni-BDC:Fc_5:1, with moderate defects, exhibited exceptional catalytic activity and stability, breaking the traditional trade-off between activity and stability. Ni-BDC:Fc_5:1 demonstrated a TOF of 0.75 O_2 s^{-1} at 1.53 V_{RHE} and required only an overpotential of 380 mV to achieve a current density of 500 mA cm^{-2}. Furthermore, both long-term CV cycles and in situ SERS revealed outstanding activity and stability. Although Ni-BDC:Fc_5:1 may eventually transform into a $NiOOH_{2-x}$-like phase, the stability of this material is remarkable and rare, given that most MOEs undergo rapid structural changes during OER. The SEIRAS showed more isolated water/OH^- in Ni-BDC:Fc_5:1, combined with Ni-BDC experienced oxygen exchange shown by isotope-labeled EC-MS, demonstrating that the defects can enhance the reactant transport and binding with internal active sites while largely preserving the local active environments. DFT calculations show that the unsaturated Ni sites effectively lower the energy gap of the RDS. As such, when applied to a real AEMWE device, this catalyst enables the realization of a cell voltage of only 1.73 V_{cell} to reach 1 A cm^{-2} and stable operation for over 120 h. This work not only develops a catalyst with significant potential for green hydrogen production but also, more importantly, demonstrates the feasibility of this concept that paves the way for designing catalytic materials that achieve a balance between activity and stability, thus contributing to the goal of zero emissions.

METHODS

Synthesis of Ni-BDC:Fc. All chemicals and solvents were used as received without further purification. 18.2 MΩ·cm Milli-Q deionized (DI) water was used in all experiments. To synthesize pure Ni-BDC, 1 mmol of $NiCl_2{\cdot}6H_2O$ (237.7 mg) was first dissolved in 16 mL of *N*,*N*-dimethylformamide (DMF) as solution A, while 1 mmol of 1,4-benzendicarboxylic acid (BDC, 166.1 mg) was dissolved in 16 mL of DMF, followed by adding 2 mL of DI water and 2 mL of ethanol as solution B. Then, solutions A and B were mixed and transferred to a 100 mL Teflon-lined stainless-steel autoclave. The autoclave was then heated for 12 h at 120 °C. For the mixed linker MOEs, different ratios of BDC (BDC was always kept at 1 mmol) and Fc acid were instead added for solution B, while the other steps were kept the same. Four ratios of BDC/Fc were selected, i.e., 10:1, 5:1, 2:1, and 1:1 during synthesis. Take Ni-BDC:Fc_5:1 as an example, 1 mmol of BDC (166.1 mg) and 0.2 mmol of Fc (46.0 mg) were dissolved in 16 mL of DMF and then 2 mL of DI water and 2 mL were added as solution B. After the reaction, the products were collected by centrifugation, washed with ethanol 3 times, and dried at 80 °C overnight. The prepared samples were denoted as their linker ratios: Ni-BDC, Ni-BDC:Fc_10:1, Ni-BDC:Fc_5:1, Ni-BDC:Fc_2:1, and Ni-BDC:Fc_1:1.

Characterization. Powder XRD (PXRD) measurements were performed using a Bruker D8-Focus Bragg−Brentano diffractometer equipped with a Cu-sealed tube (λ = 1.5418 Å) source, operating at 40 kV and 40 mA. To collect the metal weight percentage and atomic percentage in MOE, ICP-OES was employed to obtain Ni and Fe content. One milligram of MOE was soaked in 2 mL of aqua regia (3:1 ratio of HCl/HNO_3) for 24 h. One milliliter of the resulting solution was then diluted to 10 mL using DI water for elemental characterization. High-angle annular dark field STEM (HAADF-STEM) imaging was conducted using a probe-aberration corrected Thermo Fisher Scientific Themis Z G3 60−300 kV S/TEM at 200 kV. For better observation of the linkers and defects in MOEs, iDPC was used. The chemical states of elements in the synthesized products were examined by XPS using a Thermo Scientific K-Alpha+ spectrometer with monochromatic Al Kα radiation (1486.6 eV), and the binding energy of the C 1s peak at 284.6 eV was used for calibration. EPR spectrum was acquired at low temperatures (∼4.5 K). The surface area and pore size volume of the products were tested by using N_2 under 1 bar at 77 K. XANES measurements for the Ni K and Fe K edges were conducted at room temperature at the APS 12-BM and NSLS-II 7BM beamline.

Electrochemical Measurements. Electrodes were prepared by drop-casting an ink-containing catalyst powder with Nafion as the binder on a GC disk electrode (Pine Research, 5 mm diameter). Before each measurement, the GC disks were sonicated in ethanol, briefly soaked in aqua regia, and polished to a mirror finish using 0.3 μm alumina lapping sheets (Thorlabs). Inks typically consisted of 5 mg of catalyst dispersed in a 1.99 mL solution of water/ethanol (2:3 v/v) through sonication for 45 min. Ten microliter of Nafion 117 containing solution (5 wt %) was added following by sonication for 15 min. Ten microliter of resulting catalyst ink was dropped on the GC to give a nominal loading of 125 $\mu g_{catalyst}$ cm_{geo}^{-2}. A three-electrode setup was used for electrochemical measurements in a glass electrochemical cell containing O_2 saturated 100 mL 0.1 M KOH (Sigma-Aldrich, 99.99% semiconductor grade) as the supporting electrolyte. An Hg/HgO reference electrode and a carbon rod counter electrode were used. The Hg/HgO reference electrode value ($E_{Hg/HgO}$) was calibrated by averaging the potential intercepts of the hydrogen evolution and oxidation reactions during CV using a polycrystalline Pt disk working electrode at a scan rate of 10 mV s^{-1} in H_2 saturated 0.1 M KOH ($E_{Hg/HgO}$ = +0.867 V in 0.1 M KOH). A Biologic VSP-300 potentiostat was used to collect the electrochemical data. CV was performed in the electrolyte at a rotation speed of 1600 rpm from ∼1.1 V to ∼1.75 V vs RHE at a scan rate of 10 mV s^{-1}. Ohmic losses were compensated by subtracting the Ohmic drop from the measured potential by using an electrolyte resistance (R) determined by EIS. The potential after iR correction was calculated by $E_{RHE} = E_{measured} + E_{Hg/HgO} - iR$ (100% iR compensation). ECSA measurements for different BDC/Fc ratios were conducted by recording cyclic voltammograms in the non-Faradaic region (1.1 V_{RHE}−1.2 V_{RHE}) at various scan rates (20, 40, 60, 80, and 100 mV s^{-1}). Chronopotentiometry (CP) measurements were conducted to calculate the Tafel slope. Detailed information about TOF calculations can be found in Supporting Information. For catalysts loaded on NF substrate, around 2 mg Ni-BDC:Fc_5:1 or IrO_2 were loaded on NF. The electrolyte was changed to 1 M KOH to mimic the practical application. CV was carried out from ∼1 V to ∼2 V vs

https://doi.org/10.1021/jacs.5c06156
J. Am. Chem. Soc. 2025, 147, 29838−29851

RHE at a scan rate of 10 mV s^{-1}. The stability measurements were conducted using the same electrode at a current density of 500 mA cm^{-2} and monitored the potential change. When using NF as substrate, 70% *iR* correction was used for CV and CP, giving $E_{RHE} = E_{measured} + E_{Hg/HgO} - 0.70 \times iR$.

In Situ Surface-Enhanced Raman Spectroscopy. SERS was performed by using a HORIBA microscope. The Au electrode was first polished and then electrochemically roughened to create a SERS-active surface, following standard procedures (details in Supporting Information). The Au disk electrode was mounted in rotating disk electrode holders (Pine Research) and inserted into the electrochemical cell from below. A platinum wire served as the counter electrode, and a leak-free Ag/AgCl electrode (eDAQ) was used as the reference electrode. All measurements were conducted in approximately 1.5 mL of a 0.1 M KOH solution. The potential was stepped between 1.1 V_{RHE} and 1.7 V_{RHE}, with spectra collected once a steady-state current was achieved. Time-dependent spectra were gathered by holding the potential at a specific value for extended periods and recording spectra every 2 min.

In Situ Surface-Enhanced Infrared Absorption Spectroscopy. SEIRAS was conducted using a Bruker Vertex 70 Fourier-transform infrared spectrometer equipped with an MCT detector. The Au-deposited (deposition process in Supporting Information) hemispherical Si prism was mounted in a spectro-electrochemical three-electrode system. A mercury oxide electrode (Hg/HgO) and copper foil were used as the reference and counter electrodes. The SEIRAS spectra were recorded with a resolution of 4 cm^{-1} at a scan velocity of 7.5 kHz, covering the 500−4000 cm^{-1} spectral range, with an average of 64 scans. The background was collected first, then the ink of the catalyst was dropped on the Au-deposited hemispherical Si prism and dried. Five milliliter of DI water was added as the electrolyte to obtain the interfacial structure at beginning. Then, 5 mL of 2 M KOH was added to create a 1 M KOH electrolyte for collecting the interfacial structure of Ni-BDC and Ni-BDC:Fc_5:1. The in situ infrared spectra were recorded from 1.1 to 1.6 V_{RHE}.

In Situ Electrochemical Mass Spectrometer with Isotope Labeling Experiment. All electrochemical measurements with mass spectra were carried out with a commercially available microchip-based electrochemistry mass spectrometry (ECMS) setup (SpectroInlets ApS, Denmark). A 5 mm diameter GC disk decorated with the catalyst was used as the working electrode; the counter (Pt mesh) and reference (Hg/HgO) electrodes were each inserted in separate glass tubes with a ceramic frit on the tip. 0.1 M KOH in isotope-labeled $H_2{}^{18}O$ was used as the electrolyte first. The mass spectra of different species (H_2, He, H_2O, O_2, and CO_2) were recorded, while the CV of the OER was measured from ∼1.1 to 1.6 V_{RHE}. After that, the cell was washed with DI water, and the electrolyte was changed to 0.1 M KOH in $H_2{}^{16}O$ for another measurements. The loading of electrocatalyst of Ni-BDC was 12.5 $\mu g_{catalyst}$ cm_{geo}^{-2} and of Ni-BDC:Fc_5:1 was 7.5 $\mu g_{catalyst}$ cm_{geo}^{-2}.

Density Functional Theory Calculation. All spin-polarized DFT calculations were performed using the Vienna Ab initio Simulation Package (VASP)[52,53] with the projector augmented-wave approach[54] for the interaction between the ionic core and valence electrons. Electron exchange and correlation were addressed using generalized gradient approximation[55] (GGA) in the form of the Perdew−Burke−Ernzerhof (PBE) functional. The ferromagnetic initial state was used in geometry optimization for a consistent and tractable set of magnetic structures. A plane-wave basis set with an energy cutoff of 520 eV was employed. To improve the description of localized electron states, the GGA + *U* approach[56] was employed, incorporating on-site Coulomb interactions with $U - J$ values of 6.2 and 5.3 eV for Ni and Fe atoms, respectively, in accordance with the parameters used in the Materials Project.

A (1 × 2 × 3) supercell containing 132 atoms was used to study the mechanism of the OER in Ni-BDC. A Fc linker was introduced into Ni-BDC to construct Ni-BDC:Fc_5:1 containing the missing linkers. Brillouin-zone integrations were conducted using a Γ-centered 2 × 1 × 2 *k*-point grid in structural relaxation. The energy and force convergence criteria were set to be 10^{-5} eV and 0.03 eV/Å, respectively. The Gibbs free energy (G) of each elementary state at 298 K and 1 atm was calculated as

$$G = H - T\Delta S = E_{DFT} + E_{ZPE} + \int_0^{298} C_v dT - T\Delta S$$

where E_{DFT} is the electronic total energy calculated in VASP and E_{ZPE} is the zero-point vibrational energy. The spin is considered during the calculation. The enthalpy ($\int_0^{298} C_v dT$) and entropy (ΔS) contributions at room temperature were calculated from the vibrational modes of the system. The free energy of the O_2 gas molecule is extracted according to the thermodynamic energy of 4.92 eV released by the reaction of $O_2 + 4(H^+ + e^-) = 2H_2O$.

The influence of the solvation effect on the reaction thermodynamics was taken into account by employing an implicit solvent model and the VASPsol software designed based on it, wherein the bulk dielectric constant of the solvent was set to EB_K = 80 to simulate an aqueous solution environment.

Anion-Exchange Membrane Water Electrolyzer. To prepare the ink for AEMWE measurements, around 50 mg catalysts (Ni-BDC:Fc_5:1 or IrO_2) were dispersed in a mixture of 4.9 mL ethanol and 0.1 mL Nafion 117 (5 wt %) and sonicated for 2 h to form a uniform ink (∼10 mg mL^{-1}). The commercial Pt/C was used for the HER catalyst with the same ink preparation procedure. The cathodic (Pt/C) and anodic (Ni-BDC:Fc_5:1) catalysts ink were sprayed on carbon paper (Toray-060) and NF with a working area of 4 cm^2 by air-brush. The loading for Pt/C is around 1 mg cm^{-2}. The loading for Ni-BDC:Fc_5:1 or IrO_2 is 3 mg cm^{-2}. Afterward, the MEAs were fabricated by sandwiching the Sustainion® X37−50 anion-exchange membrane between the anode and cathode; followed by hot pressing at 60 °C under a pressure of 0.2 MPa for 3 min. 1 M KOH was circulated through the anodic side with a flow rate of 30 mL min^{-1} by a peristaltic pump. The electrolyte and device were put in an oven with a constant temperature of ∼65 °C. The electrolyzer was activated by using current sweeps from 0.1 A cm^{-2} (0.4 V) to 3 A cm^{-2} (12 V) with sweep intervals of 0.1 A 20 times. The polarization curves were collected by holding at different current densities and measuring the corresponding potential. The stability of the AEMWE was conducted by a CP test at 1.0 A cm^{-2} for 120 h. All measurements in AEMWE were recorded without *iR*-correction.

■ ASSOCIATED CONTENT

Supporting Information

The Supporting Information is available free of charge at https://pubs.acs.org/doi/10.1021/jacs.5c06156.

Experimental methods, synthesis, electrochemical methods and protocols; TOF calculations; PXRD patterns, XPS, EPR, BET/BJH, HAADF-STEM, electrochemical characterization, in situ Raman, and SEIRAS spectra; DOS calculation and corresponding structures; and AEMWE measurements (PDF)

■ AUTHOR INFORMATION

Corresponding Authors

Yuriy Román-Leshkov − *Department of Chemical Engineering, Massachusetts Institute of Technology, Cambridge, Massachusetts 02139, United States;* orcid.org/0000-0002-0025-4233; Email: yroman@mit.edu

Ju Li − *Department of Materials Science and Engineering, Massachusetts Institute of Technology, Cambridge, Massachusetts 02139, United States; Department of Nuclear Science and Engineering, Massachusetts Institute of Technology, Cambridge, Massachusetts 02139, United States;* orcid.org/0000-0002-7841-8058; Email: liju@mit.edu

Authors

Hongbin Xu − *Department of Materials Science and Engineering, Massachusetts Institute of Technology, Cambridge, Massachusetts 02139, United States;* orcid.org/0009-0007-6311-475X

Daniel J. Zheng − *Department of Materials Science and Engineering, Massachusetts Institute of Technology, Cambridge, Massachusetts 02139, United States;* orcid.org/0000-0002-9471-6856

Shuo Wang − *Ningbo Key Laboratory of All-Solid-State Battery, Ningbo Institute of Digital Twin, Eastern Institute for Advanced Study, Eastern Institute of Technology, Ningbo, Zhejiang 315200, P. R. China;* orcid.org/0000-0002-7907-9676

Ethan Yupeng Zheng − *Department of Materials Science and Engineering, Massachusetts Institute of Technology, Cambridge, Massachusetts 02139, United States;* orcid.org/0009-0007-5536-285X

Yilin Zhang − *Ningbo Key Laboratory of All-Solid-State Battery, Ningbo Institute of Digital Twin, Eastern Institute for Advanced Study, Eastern Institute of Technology, Ningbo, Zhejiang 315200, P. R. China*

Tongchao Liu − *Chemical Sciences and Engineering Division, Argonne National Laboratory, Lemont, Illinois 60439, United States;* orcid.org/0000-0002-6010-3891

Junxiang Liu − *Chemical Sciences and Engineering Division, Argonne National Laboratory, Lemont, Illinois 60439, United States;* orcid.org/0000-0002-8256-1770

Davide Menga − *Research Laboratory of Electronics, Massachusetts Institute of Technology, Cambridge, Massachusetts 02139, United States*

Junghwa Kim − *Department of Materials Science and Engineering, Massachusetts Institute of Technology, Cambridge, Massachusetts 02139, United States;* orcid.org/0000-0002-2615-963X

Jen-Hung Fang − *Department of Materials Science and Engineering, Massachusetts Institute of Technology, Cambridge, Massachusetts 02139, United States;* orcid.org/0000-0001-8665-4088

Xiao Wang − *Department of Chemical Engineering, Massachusetts Institute of Technology, Cambridge, Massachusetts 02139, United States;* orcid.org/0000-0003-1624-8230

Zhen Zhang − *Department of Materials Science and Engineering, Massachusetts Institute of Technology, Cambridge, Massachusetts 02139, United States*

Lena Schröck − *Research Laboratory of Electronics, Massachusetts Institute of Technology, Cambridge, Massachusetts 02139, United States*

Jiaqi Wang − *X-ray Science Division, Advanced Photon Source, Argonne National Laboratory, Lemont, Illinois 60439, United States;* orcid.org/0000-0003-1176-704X

Sungsik Lee − *X-ray Science Division, Advanced Photon Source, Argonne National Laboratory, Lemont, Illinois 60439, United States;* orcid.org/0000-0002-1425-9852

Sunmoon Yu − *Research Laboratory of Electronics, Massachusetts Institute of Technology, Cambridge, Massachusetts 02139, United States;* orcid.org/0000-0001-7250-9365

Haldrian Iriawan − *Department of Materials Science and Engineering, Massachusetts Institute of Technology, Cambridge, Massachusetts 02139, United States;* orcid.org/0000-0002-2997-1180

Guanzhou Zhu − *Department of Nuclear Science and Engineering, Massachusetts Institute of Technology, Cambridge, Massachusetts 02139, United States*

Yang Shao-Horn − *Department of Materials Science and Engineering, Massachusetts Institute of Technology, Cambridge, Massachusetts 02139, United States; Research Laboratory of Electronics and Department of Mechanical Engineering, Massachusetts Institute of Technology, Cambridge, Massachusetts 02139, United States;* orcid.org/0000-0001-8714-2121

Complete contact information is available at: https://pubs.acs.org/10.1021/jacs.5c06156

Author Contributions

○H.X. and D.J.Z. authors contributed equally.

Notes

The authors declare no competing financial interest.

■ ACKNOWLEDGMENTS

This work was supported in part by the DOE-BES through the Energy Frontier Research Center (DE-SC0023415) (Center for Electrochemical Dynamics and Reaction on Surfaces) and MIT Climate Grand Challenge-Center for Electrification and Decarbonization of Industry (MIT-CEDI). This work made use of the Materials Research Laboratory Shared Experimental Facilities at the Massachusetts Institute of Technology. This work was carried out in part through the use of MIT.nano's facilities. This work was performed in part at the Center for Nanoscale Systems of Harvard University. This research was performed on APS beam time award(s) (https://doi.org/10.46936/APS-190029/60014112) from the Advanced Photon Source, a U.S. Department of Energy (DOE) Office of Science user facility at Argonne National Laboratory, and is based on research supported by the U.S. DOE Office of Science-Basic Energy Sciences, under Contract No. DE-AC02-06CH11357. This work gratefully acknowledges support from the U.S. Department of Energy (DOE), Office of Energy Efficiency and Renewable Energy, Vehicle Technologies Office. Thank Yiming Rao for the support and discussion.

■ REFERENCES

(1) Xie, H.; Zhao, Z.; Liu, T.; Wu, Y.; Lan, C.; Jiang, W.; Zhu, L.; Wang, Y.; Yang, D.; Shao, Z. A Membrane-Based Seawater Electrolyser for Hydrogen Generation. *Nature* **2022**, *612* (7941), 673−678.

(2) Wang, J.; Gao, Y.; Kong, H.; Kim, J.; Choi, S.; Ciucci, F.; Hao, Y.; Yang, S.; Shao, Z.; Lim, J. Non-Precious-Metal Catalysts for Alkaline Water Electrolysis: *Operando* Characterizations, Theoretical Calculations, and Recent Advances. *Chem. Soc. Rev.* **2020**, *49* (24), 9154−9196.

(3) Chong, L.; Gao, G.; Wen, J.; Li, H.; Xu, H.; Green, Z.; Sugar, J. D.; Kropf, A. J.; Xu, W.; Lin, X.-M.; Xu, H.; Wang, L.-W.; Liu, D.-J. La- and Mn-Doped Cobalt Spinel Oxygen Evolution Catalyst for Proton Exchange Membrane Electrolysis. *Science* **2023**, *380* (6645), 609−616.

(4) Li, Z.; Lin, G.; Wang, L.; Lee, H.; Du, J.; Tang, T.; Ding, G.; Ren, R.; Li, W.; Cao, X.; Ding, S.; Ye, W.; Yang, W.; Sun, L. Seed-Assisted Formation of NiFe Anode Catalysts for Anion Exchange Membrane Water Electrolysis at Industrial-Scale Current Density. *Nat. Catal.* **2024**, *7* (8), 944−952.

(5) Wu, Z.-Y.; Chen, F.-Y.; Li, B.; Yu, S.-W.; Finfrock, Y. Z.; Meira, D. M.; Yan, Q.-Q.; Zhu, P.; Chen, M.-X.; Song, T.-W.; Yin, Z.; Liang, H.-W.; Zhang, S.; Wang, G.; Wang, H. Non-Iridium-Based Electrocatalyst for Durable Acidic Oxygen Evolution Reaction in Proton

Exchange Membrane Water Electrolysis. *Nat. Mater.* **2023**, *22* (1), 100−108.
(6) Chen, Y.; Li, Q.; Lin, Y.; Liu, J.; Pan, J.; Hu, J.; Xu, X. Boosting Oxygen Evolution Reaction by FeNi Hydroxide-Organic Framework Electrocatalyst toward Alkaline Water Electrolyzer. *Nat. Commun.* **2024**, *15* (1), 7278.
(7) Lyu, S.; Guo, C.; Wang, J.; Li, Z.; Yang, B.; Lei, L.; Wang, L.; Xiao, J.; Zhang, T.; Hou, Y. Exceptional Catalytic Activity of Oxygen Evolution Reaction via Two-Dimensional Graphene Multilayer Confined Metal-Organic Frameworks. *Nat. Commun.* **2022**, *13* (1), 6171.
(8) Zhu, W.; Song, X.; Liao, F.; Huang, H.; Shao, Q.; Feng, K.; Zhou, Y.; Ma, M.; Wu, J.; Yang, H.; Yang, H.; Wang, M.; Shi, J.; Zhong, J.; Cheng, T.; Shao, M.; Liu, Y.; Kang, Z. Stable and Oxidative Charged Ru Enhance the Acidic Oxygen Evolution Reaction Activity in Two-Dimensional Ruthenium-Iridium Oxide. *Nat. Commun.* **2023**, *14* (1), 5365.
(9) Chen, F.-Y.; Wu, Z.-Y.; Adler, Z.; Wang, H. Stability Challenges of Electrocatalytic Oxygen Evolution Reaction: From Mechanistic Understanding to Reactor Design. *Joule* **2021**, *5* (7), 1704−1731.
(10) Chung, D. Y.; Lopes, P. P.; Farinazzo Bergamo Dias Martins, P.; He, H.; Kawaguchi, T.; Zapol, P.; You, H.; Tripkovic, D.; Strmcnik, D.; Zhu, Y.; Seifert, S.; Lee, S.; Stamenkovic, V. R.; Markovic, N. M. Dynamic Stability of Active Sites in Hydr(Oxy)-Oxides for the Oxygen Evolution Reaction. *Nat. Energy* **2020**, *5* (3), 222−230.
(11) Peng, L.; Yang, N.; Yang, Y.; Wang, Q.; Xie, X.; Sun-Waterhouse, D.; Shang, L.; Zhang, T.; Waterhouse, G. I. N. Atomic Cation-Vacancy Engineering of NiFe-Layered Double Hydroxides for Improved Activity and Stability towards the Oxygen Evolution Reaction. *Angew. Chem., Int. Ed.* **2021**, *60* (46), 24612−24619.
(12) Oener, S. Z.; Bergmann, A.; Cuenya, B. R. Designing Active Oxides for a Durable Oxygen Evolution Reaction. *Nat. Synth.* **2023**, *2* (9), 817−827.
(13) Zhai, P.; Wang, C.; Zhao, Y.; Zhang, Y.; Gao, J.; Sun, L.; Hou, J. Regulating Electronic States of Nitride/Hydroxide to Accelerate Kinetics for Oxygen Evolution at Large Current Density. *Nat. Commun.* **2023**, *14* (1), 1873.
(14) Xu, H.; Jia, H.; Fei, B.; Ha, Y.; Li, H.; Guo, Y.; Liu, M.; Wu, R. Charge Transfer Engineering via Multiple Heteroatom Doping in Dual Carbon-Coupled Cobalt Phosphides for Highly Efficient Overall Water Splitting. *Appl. Catal., B* **2020**, *268*, 118404.
(15) Zhou, D.; Li, P.; Lin, X.; McKinley, A.; Kuang, Y.; Liu, W.; Lin, W.-F.; Sun, X.; Duan, X. Layered Double Hydroxide-Based Electrocatalysts for the Oxygen Evolution Reaction: Identification and Tailoring of Active Sites, and Superaerophobic Nanoarray Electrode Assembly. *Chem. Soc. Rev.* **2021**, *50* (15), 8790−8817.
(16) Liu, D.; Yan, X.; Guo, P.; Yang, Y.; He, Y.; Liu, J.; Chen, J.; Pan, H.; Wu, R. Inert Mg Incorporation to Break the Activity/Stability Relationship in High-Entropy Layered Hydroxides for the Electrocatalytic Oxygen Evolution Reaction. *ACS Catal.* **2023**, *13* (11), 7698−7706.
(17) Anantharaj, S.; Karthik, P. E.; Noda, S. The Significance of Properly Reporting Turnover Frequency in Electrocatalysis Research. *Angew. Chem., Int. Ed.* **2021**, *60* (43), 23051−23067.
(18) Wei, J.; Tang, H.; Sheng, L.; Wang, R.; Fan, M.; Wan, J.; Wu, Y.; Zhang, Z.; Zhou, S.; Zeng, J. Site-Specific Metal-Support Interaction to Switch the Activity of Ir Single Atoms for Oxygen Evolution Reaction. *Nat. Commun.* **2024**, *15* (1), 559.
(19) Dau, H.; Limberg, C.; Reier, T.; Risch, M.; Roggan, S.; Strasser, P. The Mechanism of Water Oxidation: From Electrolysis via Homogeneous to Biological Catalysis. *ChemCatChem* **2010**, *2* (7), 724−761.
(20) Xue, Z.; Liu, K.; Liu, Q.; Li, Y.; Li, M.; Su, C.-Y.; Ogiwara, N.; Kobayashi, H.; Kitagawa, H.; Liu, M.; Li, G. Missing-Linker Metal-Organic Frameworks for Oxygen Evolution Reaction. *Nat. Commun.* **2019**, *10* (1), 5048.
(21) Kuai, C.; Xu, Z.; Xi, C.; Hu, A.; Yang, Z.; Zhang, Y.; Sun, C.-J.; Li, L.; Sokaras, D.; Dong, C.; Qiao, S.-Z.; Du, X.-W.; Lin, F. Phase Segregation Reversibility in Mixed-Metal Hydroxide Water Oxidation Catalysts. *Nat. Catal.* **2020**, *3* (9), 743−753.
(22) Xu, H.; Zheng, D. J.; Iriawan, H.; Fang, J.-H.; Kim, J.; Wang, X.; Román-Leshkov, Y.; Li, J.; Shao-Horn, Y. A Cobalt−Platinum−Ruthenium System for Acidic Methanol Oxidation. *Chem. Mater.* **2024**, *36* (14), 6938−6949.
(23) Xu, H.; Jia, H.; Li, H.; Liu, J.; Gao, X.; Zhang, J.; Liu, M.; Sun, D.; Chou, S.; Fang, F.; Wu, R. Dual Carbon-Hosted Co-N3 Enabling Unusual Reaction Pathway for Efficient Oxygen Reduction Reaction. *Appl. Catal., B* **2021**, *297*, 120390.
(24) Zhao, S.; Wang, Y.; Dong, J.; He, C.-T.; Yin, H.; An, P.; Zhao, K.; Zhang, X.; Gao, C.; Zhang, L.; Lv, J.; Wang, J.; Zhang, J.; Khattak, A. M.; Khan, N. A.; Wei, Z.; Zhang, J.; Liu, S.; Zhao, H.; Tang, Z. Ultrathin Metal−Organic Framework Nanosheets for Electrocatalytic Oxygen Evolution. *Nat. Energy* **2016**, *1* (12), 16184.
(25) Hanikel, N.; Pei, X.; Chheda, S.; Lyu, H.; Jeong, W.; Sauer, J.; Gagliardi, L.; Yaghi, O. M. Evolution of Water Structures in Metal-Organic Frameworks for Improved Atmospheric Water Harvesting. *Science* **2021**, *374* (6566), 454−459.
(26) Yuan, S.; Peng, J.; Cai, B.; Huang, Z.; Garcia-Esparza, A. T.; Sokaras, D.; Zhang, Y.; Giordano, L.; Akkiraju, K.; Zhu, Y. G.; Hübner, R.; Zou, X.; Román-Leshkov, Y.; Shao-Horn, Y. Tunable Metal Hydroxide−Organic Frameworks for Catalysing Oxygen Evolution. *Nat. Mater.* **2022**, *21* (6), 673−680.
(27) Zheng, D. J.; Görlin, M.; McCormack, K.; Kim, J.; Peng, J.; Xu, H.; Ma, X.; LeBeau, J. M.; Fischer, R. A.; Román-Leshkov, Y.; Shao-Horn, Y. Linker-Dependent Stability of Metal-Hydroxide Organic Frameworks for Oxygen Evolution. *Chem. Mater.* **2023**, *35* (13), 5017−5031.
(28) Yang, C.; Rousse, G.; Louise Svane, K.; Pearce, P. E.; Abakumov, A. M.; Deschamps, M.; Cibin, G.; Chadwick, A. V.; Dalla Corte, D. A.; Anton Hansen, H.; Vegge, T.; Tarascon, J.-M.; Grimaud, A. Cation Insertion to Break the Activity/Stability Relationship for Highly Active Oxygen Evolution Reaction Catalyst. *Nat. Commun.* **2020**, *11* (1), 1378.
(29) Hong, W. T.; Risch, M.; Stoerzinger, K. A.; Grimaud, A.; Suntivich, J.; Shao-Horn, Y. Toward the Rational Design of Non-Precious Transition Metal Oxides for Oxygen Electrocatalysis. *Energy Environ. Sci.* **2015**, *8* (5), 1404−1427.
(30) Li, W.; Wang, D.; Zhang, Y.; Tao, L.; Wang, T.; Zou, Y.; Wang, Y.; Chen, R.; Wang, S. Defect Engineering for Fuel-Cell Electrocatalysts. *Adv. Mater.* **2020**, *32* (19), 1907879.
(31) Zhang, Y.; Liu, J.; Xu, Y.; Xie, C.; Wang, S.; Yao, X. Design and Regulation of Defective Electrocatalysts. *Chem. Soc. Rev.* **2024**, *53*, 10620.
(32) Görlin, M.; Halldin Stenlid, J.; Koroidov, S.; Wang, H.-Y.; Börner, M.; Shipilin, M.; Kalinko, A.; Murzin, V.; Safonova, O. V.; Nachtegaal, M.; Uheida, A.; Dutta, J.; Bauer, M.; Nilsson, A.; Diaz-Morales, O. Key Activity Descriptors of Nickel-Iron Oxygen Evolution Electrocatalysts in the Presence of Alkali Metal Cations. *Nat. Commun.* **2020**, *11* (1), 6181.
(33) Jiang, Y.; Deng, Y.-P.; Liang, R.; Fu, J.; Gao, R.; Luo, D.; Bai, Z.; Hu, Y.; Yu, A.; Chen, Z. D-Orbital Steered Active Sites through Ligand Editing on Heterometal Imidazole Frameworks for Rechargeable Zinc-Air Battery. *Nat. Commun.* **2020**, *11* (1), 5858.
(34) Cai, G.; Jiang, H. A Modulator-Induced Defect-Formation Strategy to Hierarchically Porous Metal−Organic Frameworks with High Stability. *Angew. Chem., Int. Ed.* **2017**, *56* (2), 563−567.
(35) Alobaid, A.; Wang, C.; Adomaitis, R. A. Mechanism and Kinetics of HER and OER on NiFe LDH Films in an Alkaline Electrolyte. *J. Electrochem. Soc.* **2018**, *165* (15), J3395−J3404.
(36) Shinagawa, T.; Garcia-Esparza, A. T.; Takanabe, K. Insight on Tafel Slopes from a Microkinetic Analysis of Aqueous Electrocatalysis for Energy Conversion. *Sci. Rep.* **2015**, *5*, 13801.
(37) Zheng, W.; Lee, L. Y. S. Metal−Organic Frameworks for Electrocatalysis: Catalyst or Precatalyst? *ACS Energy Lett.* **2021**, *6* (8), 2838−2843.

(38) Lee, S.; Bai, L.; Hu, X. Deciphering Iron-Dependent Activity in Oxygen Evolution Catalyzed by Nickel−Iron Layered Double Hydroxide. *Angew. Chem., Int. Ed.* **2020**, *59* (21), 8072−8077.
(39) Klaus, S.; Cai, Y.; Louie, M. W.; Trotochaud, L.; Bell, A. T. Effects of Fe Electrolyte Impurities on Ni(OH) $_2$/NiOOH Structure and Oxygen Evolution Activity. *J. Phys. Chem. C* **2015**, *119* (13), 7243−7254.
(40) Zhang, B.; Zheng, X.; Voznyy, O.; Comin, R.; Bajdich, M.; García-Melchor, M.; Han, L.; Xu, J.; Liu, M.; Zheng, L.; García De Arquer, F. P.; Dinh, C. T.; Fan, F.; Yuan, M.; Yassitepe, E.; Chen, N.; Regier, T.; Liu, P.; Li, Y.; De Luna, P.; Janmohamed, A.; Xin, H. L.; Yang, H.; Vojvodic, A.; Sargent, E. H. Homogeneously Dispersed Multimetal Oxygen-Evolving Catalysts. *Science* **2016**, *352* (6283), 333−337.
(41) Pan, Y.; Xu, X.; Zhong, Y.; Ge, L.; Chen, Y.; Veder, J.-P. M.; Guan, D.; O'Hayre, R.; Li, M.; Wang, G.; Wang, H.; Zhou, W.; Shao, Z. Direct Evidence of Boosted Oxygen Evolution over Perovskite by Enhanced Lattice Oxygen Participation. *Nat. Commun.* **2020**, *11* (1), 2002.
(42) Han, B.; Stoerzinger, K. A.; Tileli, V.; Gamalski, A. D.; Stach, E. A.; Shao-Horn, Y. Nanoscale Structural Oscillations in Perovskite Oxides Induced by Oxygen Evolution. *Nat. Mater.* **2017**, *16* (1), 121−126.
(43) Huang, B.; Rao, R. R.; You, S.; Hpone Myint, K.; Song, Y.; Wang, Y.; Ding, W.; Giordano, L.; Zhang, Y.; Wang, T.; Muy, S.; Katayama, Y.; Grossman, J. C.; Willard, A. P.; Xu, K.; Jiang, Y.; Shao-Horn, Y. Cation- and pH-Dependent Hydrogen Evolution and Oxidation Reaction Kinetics. *JACS Au* **2021**, *1* (10), 1674−1687.
(44) Montoro, C.; Ocón, P.; Zamora, F.; Navarro, J. A. R. Metal−Organic Frameworks Containing Missing-Linker Defects Leading to High Hydroxide-Ion Conductivity. *Chem.—Eur. J.* **2016**, *22* (5), 1646−1651.
(45) Murata, K.; Mitsuoka, K.; Hirai, T.; Walz, T.; Agre, P.; Heymann, J. B.; Engel, A.; Fujiyoshi, Y. Structural Determinants of Water Permeation through Aquaporin-1. *Nature* **2000**, *407* (6804), 599−605.
(46) Fan, K.; Chen, H.; Ji, Y.; Huang, H.; Claesson, P. M.; Daniel, Q.; Philippe, B.; Rensmo, H.; Li, F.; Luo, Y.; Sun, L. Nickel−Vanadium Monolayer Double Hydroxide for Efficient Electrochemical Water Oxidation. *Nat. Commun.* **2016**, *7* (1), 11981.
(47) Hou, Z.; Xiang, D.; Yang, D.; Wen, L.; Luo, H.; Li, L.; Yang, Q.; Hu, L. Electrical and Structural Optimization of Nickel Sulfide Nano-Flower by Mn Modulation as Robust Bifunctional Electrocatalyst for Overall Water Splitting. *J. Electrochem. Soc.* **2022**, *169* (10), 106512.
(48) Louie, M. W.; Bell, A. T. An Investigation of Thin-Film Ni−Fe Oxide Catalysts for the Electrochemical Evolution of Oxygen. *J. Am. Chem. Soc.* **2013**, *135* (33), 12329−12337.
(49) Yu, P.-C.; Zhang, X.-L.; Zhang, T.-Y.; Tao, X.-Y.-N.; Yang, Y.; Wang, Y.-H.; Zhang, S.-C.; Gao, F.-Y.; Niu, Z.-Z.; Fan, M.-H.; Gao, M.-R. Nitrogen-Mediated Promotion of Cobalt-Based Oxygen Evolution Catalyst for Practical Anion-Exchange Membrane Electrolysis. *J. Am. Chem. Soc.* **2024**, *146* (29), 20379−20390.
(50) U.S. Department of Energy. *Technical Targets for Liquid Alkaline Electrolysis*. https://www.energy.gov/eere/fuelcells/technical-targets-liquid-alkaline-electrolysis.
(51) Li, Z.; Lin, G.; Wang, L.; Lee, H.; Du, J.; Tang, T.; Ding, G.; Ren, R.; Li, W.; Cao, X.; Ding, S.; Ye, W.; Yang, W.; Sun, L. Seed-Assisted Formation of NiFe Anode Catalysts for Anion Exchange Membrane Water Electrolysis at Industrial-Scale Current Density. *Nat. Catal.* **2024**, *7* (8), 944−952.
(52) Kresse, G.; Hafner, J. *Ab Initio* Molecular Dynamics for Liquid Metals. *Phys. Rev. B* **1993**, *47* (1), 558−561.
(53) Kresse, G.; Furthmüller, J. Efficient Iterative Schemes for *Ab Initio* Total-Energy Calculations Using a Plane-Wave Basis Set. *Phys. Rev. B* **1996**, *54* (16), 11169−11186.
(54) Blöchl, P. E. Projector Augmented-Wave Method. *Phys. Rev. B* **1994**, *50* (24), 17953−17979.
(55) Perdew, J. P.; Burke, K.; Ernzerhof, M. Generalized Gradient Approximation Made Simple. *Phys. Rev. Lett.* **1996**, *77* (18), 3865−3868.
(56) Dudarev, S. L.; Botton, G. A.; Savrasov, S. Y.; Humphreys, C. J.; Sutton, A. P. Electron-Energy-Loss Spectra and the Structural Stability of Nickel Oxide: An LSDA+U Study. *Phys. Rev. B* **1998**, *57* (3), 1505−1509.

https://doi.org/10.1021/jacs.5c06156
J. Am. Chem. Soc. 2025, 147, 29838−29851